Solid Earth, 14, 551–570, 2023
https://doi.org/10.5194/se-14-551-2023

Solid Earth Open Access EGU

Kinematics and time-resolved evolution of the main thrust-sense shear zone in the Eo-Alpine orogenic wedge (the Vinschgau Shear Zone, eastern Alps)

Chiara Montemagni[1], Stefano Zanchetta[1], Martina Rocca[1], Igor M. Villa[1], Corrado Morelli[2], Volkmar Mair[2], and Andrea Zanchi[1]

[1]Dipartimento di Scienze dell'Ambiente e della Terra, Università degli Studi di Milano – Bicocca, 20126 Milan, Italy
[2]Ufficio Geologia e Prove Materiali, Provincia Autonoma di Bolzano Alto Adige, 39053 Cardano, Italy

Correspondence: Chiara Montemagni (chiara.montemagni@unimib.it)

Received: 30 January 2023 – Discussion started: 6 February 2023
Revised: 26 April 2023 – Accepted: 26 April 2023 – Published: 24 May 2023

Abstract. The Vinschgau Shear Zone (VSZ) is one of the largest and most significant shear zones developed under plastic conditions within the Austroalpine domain, juxtaposing the Ötztal and the Texel units to the Campo, Scharl and Sesvenna units during the building of the Eo-Alpine Orogen. The VSZ dominates the structural setting of a large portion of the central Austroalpine Late Cretaceous thrust stack. In order to fully assess the evolution of the VSZ, a multifaceted approach based on detailed multiscale structural and petrochronological analyses has been carried out across representative transects of the shear zone in the Vinschgau Valley. The research has been performed with a view to characterizing kinematics, P–T conditions and timing of motion of the VSZ.

Our fieldwork-based analyses suggest that the dip angle of mylonitic foliation increases from west to east with an E–W-trending stretching lineation which dips alternatively to the west and to the east, due to later folding related to the Cenozoic crustal shortening. The dominant top-to-W shear sense of the mylonites recognized in the field and confirmed by microstructural analyses led to exhumation of the upper Austroalpine nappes in the hanging wall of the shear zone; the Texel unit with Late Cretaceous eclogites and the Schneeberg and Ötztal units were all affected by Eo-Alpine amphibolite-facies metamorphism. Chemical and microstructural analyses suggest deformation temperatures of ca. 350–400 °C during shearing. Timing of deformation along the VSZ has been constrained for the first time through $^{40}Ar/^{39}Ar$ dating of syn-shearing micas, which reveal a Late Cretaceous age of the VSZ mylonites with ages ranging between 80 and 97 Ma. A systematic younging age of deformation occurs towards the central part of the shear zone in the studied transects. Vorticity analysis shows a clear decrease in the simple shear component correlated to the younging of mica ages towards the core of the shear zone. This evolution is consistent with the growth of a shear zone where shear strain localizes into its central part during deformation. The defined evolution of the VSZ sheds new light on how large-scale thrust-sense shear zones act and how much exhumation they can accommodate in the frame of an evolving orogenic wedge.

1 Introduction

The Vinschgau Shear Zone (VSZ), extending along the homonymous valley (NE Italy; Fig. 1a–b), is one of the most important tectonic structures developed within the Austroalpine domain of the Alps (Figs. 1 and 2). Starting from the first systematic studies of the Alpine belt, this large shear zone, firstly defined as the "Schlinig Thrust", was interpreted as a top-to-W thrust plane (Spitz and Dyhrenfurth, 1914). Although several authors later rejected this interpretation (Heim, 1922; Staub, 1937), modern studies (Schmid and Haas, 1989; Froitzheim et al., 1994, 1997) carried out since the end of the last century demonstrated the validity of the first assumptions. Recent structural analyses (Brunel, 1980; Ratschbacher, 1986; Ratschbacher et al., 1989; Schmid and Haas, 1989; Pomella et al., 2016) recognized indeed

that the entire central Austroalpine nappe stack was affected by W-directed tectonic transport during the first stages of the Late Cretaceous Alpine deformations. Along the VSZ, the Austroalpine tectonometamorphic units with a dominant metamorphism of Alpine age overthrust Austroalpine units (Sesvenna and Campo–Ortler) that were only slightly affected by Alpine metamorphism (up to greenschist facies) and deformation during the Eo-Alpine stage (Thöni, 1981), still largely preserving features acquired during the Variscan orogeny.

The VSZ is almost continuously exposed for more than 50 km, mainly on the northern flank of the Vinschgau Valley (Fig. 1), reaching a maximum thickness of about 550 m close to Eyrs (Figs. 1 and 2). These features make the VSZ one of the largest ductile thrust-sense shear zones now exposed in the Alps, together with the Periadriatic Fault (Schmid et al., 1987; 1989) and the Orobic Thrust in the southern Alps (Zanchetta et al., 2011; D'Adda and Zanchetta, 2015). The Noric Thrust in the eastern Alps (Ratschbacher, 1986) is another important ductile thrust, the first one studied by modern kinematic and structural methods. Due to its complete exposure and accessibility, the prominent VSZ represents an ideal natural laboratory for the study of cumulative shear strain distribution during the development of a large mature intra-basement shear zone and to evaluate the evolution in terms of shear strain localization, coaxiality, kinematic and lifetime of activity (e.g., Xypolias, 2010; Xypolias and Koukouvelas, 2001; Law et al., 2013; Fossen and Cavalcante, 2017; Oriolo et al., 2016, 2018).

Large-scale thrust- or normal-sense shear zones developed within collisional settings display huge along-strike exposures such as the ca. 2500 km of the Main Central Thrust and South Tibetan Detachment in the Himalayan orogen (e.g., Caby et al., 1983; Searle et al., 2008), the ca. 30 km of the Simplon Shear Zone (Mancktelow, 1985) and Brenner Fault (Rosenberg et al., 2018) in the Alps, or the Great Slave Lake shear zone (Hanmer et al., 1992) in northern Canada. Due to its peculiar exposure along the strike, the VSZ shows different features from shallow depth conditions in its western portion and deeper conditions at the eastern end (Schmid and Haas, 1989), providing a complete crustal section of a large-scale shear zone. This kind of exposure provides insights not only on the different deformation mechanisms and behaviors of the shear zone at different crustal levels, but also on its evolution through time.

In this work, we applied a quantitative approach to reconstruct the evolution through space (depth) and time of the VSZ. $^{40}Ar/^{39}Ar$ dating of syn-mylonitic micas sampled along several transects of the VSZ have been combined with microstructural and mineralogical analyses, aimed to define the P–T condition of shearing. The analysis of the cumulative shear strain distribution and the kinematic vorticity of flow (e.g., Montemagni and Zanchetta, 2022; Petroccia et al., 2022) finally provides a full kinematic and time-resolved evolution of the VSZ that could be taken as an example of how a regional-scale thrust-sense shear zone develops within a collisional orogen.

2 Geological setting

The study area (Figs. 1 and 2) is located along the Vinschgau Valley (NE Italy), entirely extending within the central Austroalpine domain, between the northern Calcareous Alps to the north and the Periadriatic Fault to the south (Fig. 1). Here, the Austroalpine domain consists of tectonometamorphic units that have been identified based on paragenesis, deformation history, metamorphism and relative ages. These units are the Pejo and Laas units (belonging to the Campo–Ortler nappe system) and the Ötztal–Stubai complex, the Matsch unit, and finally the Texel and the Schneeberg units (belonging to the Koralpe–Wölz high-pressure nappe system; Schmid et al., 2004; Handy et al., 2010; Pomella et al., 2016; Klug and Froitzheim, 2022). The E–W-striking VSZ separates the Pejo and Laas units to the south, the footwall of the VSZ characterized by greenschist-facies Alpine metamorphism, from the Ötztal, Matsch, Texel and Schneeberg units forming the hanging wall, characterized by amphibolite- to eclogite-facies Alpine metamorphism (Fig. 2). Therefore, the VSZ together with the Passeier Fault, the Jaufen Fault and the Defereggen–Antholz–Vals Fault (PSF, JF and DAV in Fig. 1) has been considered to form the southern limit of Alpine metamorphism (SAM; Hoinkes et al., 1999), a large fault system defining the southern border of the high-grade Alpine metamorphism in the Austroalpine domain of the eastern Alps.

The VSZ has been described as a ductile-to-brittle fault formed by a thick zone of mylonites and phyllonites exposed mainly along the left hydrographic side of the Vinschgau Valley (Fig. 2; Schmid and Haas, 1989; Conti, 1997; Froitzheim et al., 1997; Thöni, 1999; Sölva et al., 2005; Pomella et al., 2016; Koltai et al., 2018; Klug and Froitzheim, 2022). Schmid and Haas (1989) defined the main structure as a thick intra-basement shear zone dominated by intracrystalline plastic processes, showing different thermal conditions ranging from 300 °C to the west up to 500 °C to the east. The VSZ forms a wide system of shear zones, branching out eastward across the folded boundaries between the Ordovician Partschinser Granodiorite (also named Tschigot orthogneiss; Zantedeschi, 1991) and the host paragneiss of the Texel unit. The VSZ shows a gently N-dipping foliation (20–30°) and a constantly E–W-trending lineation, with kinematic indicators at the mesoscopic and microstructural scale that point to a top-to-NNW sense of shear (Schmid and Haas, 1989).

Four tectonic units mainly consisting of polyphase metamorphic crystalline basement rocks, which were deeply involved in the Alpine deformation and metamorphism, form the hanging wall of the shear zone. They consist of the western termination of the Texel and Schneeberg units and of the

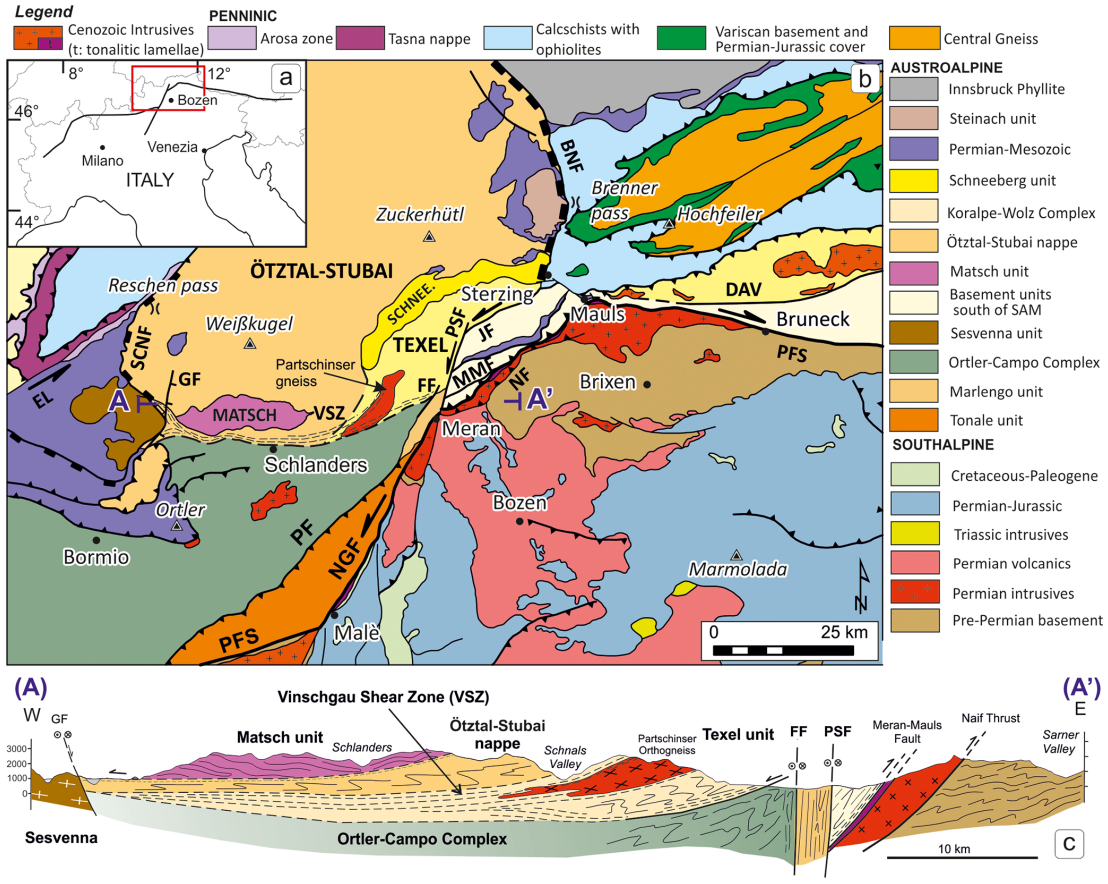

Figure 1. Geological setting of the eastern–central Alps. **(a)** N Italy, location of the study area, is marked with a red box. **(b)** Tectonic scheme of the eastern–central Alps (modified after Schmid et al., 2004; Pomella et al., 2016). **(c)** The cross-section, trace A-A′ in panel **(a)**, has been drawn in a larger scale with respect to the tectonic scheme. BNF: Brenner Normal Fault; DAV: Defereggen–Antholz–Vals Fault; EL: Engadine Line; FF: Forst Fault; GF: Glurns Fault; JF: Jaufen Fault; NGF: North Giudicarie Fault; PF: Pejo Fault; PFS: Periadriatic Fault; PSF: Passeier Fault; SCNF: Schlinig Normal Fault; VSZ: Vinschgau Shear Zone.

Ötztal unit, one of the largest nappes of the Late Cretaceous Austroalpine thrust stack, which is overthrust by the Matsch unit, forming a folded klippe atop the VSZ mylonites.

The age pattern of the Alpine metamorphic peak of the tectonometamorphic units in the hanging wall of the VSZ displays almost coeval ages in the Texel and the Schneeberg units. Partially amphibolitized eclogite boudins, preserved within the mica schists and paragneisses of the Texel unit, point to metamorphic peak conditions during the Alpine orogenesis of 540–630 °C and 1.2–1.4 GPa (Habler et al., 2006), with even higher temperature and pressure suggested for other eclogite occurrences (Poli, 1991; Zanchetta et al., 2012, 2013). Peak metamorphic conditions close to the amphibolite–eclogite facies boundary have been suggested for the Schneeberg unit, with a peak temperature of 550–600 °C and a pressure of 0.8–1.0 Gpa (Konzett and Hoinkes, 1996; Krenn et al., 2011). Geochronological data in the literature point to a Late Cretaceous age for both the Texel eclogites (U–Pb zircon ages of 84 ± 5 Ma; Habler et al., 2006; Zanchetta et al., 2013) and the upper-amphibolite-facies metamorphism of the Schneeberg unit, for which ages ranging between 85–86 Ma ($^{40}Ar/^{39}Ar$ age on paragonitic white mica in amphibolites; Konzett and Hoinkes, 1996) and 90.9 ± 4.1 Ma (Sm–Nd on garnet cores in metapelites; Sölva et al., 2005) have been obtained.

The age and the peak metamorphic conditions experienced by the Ötztal unit during the Alpine metamorphism are far less constrained. Mid-Cretaceous to Late Cretaceous K–Ar mica ages (100–110 Ma) have been obtained by Thöni (1980) from the basement in the hanging wall of the VSZ, and a whole-rock Rb–Sr age of 83 ± 1 Ma resulted from a metapegmatite of the Matsch unit (Fig. 2) at the western end of the VSZ (Thöni, 1986). An Alpine age of upper-greenschist-facies metamorphism in the Matsch unit has also been argued by Habler et al. (2009), on the basis of Early to Middle Permian intrusion age of pegmatites, which were later deformed and metamorphosed, and the growth of chloritoid after pre-Alpine staurolite. The Alpine metamorphism in the Ötztal unit reached 530–550 °C in the southeastern part (Purtscheller and Rammlmair, 1982; Hoinkes et al., 1999),

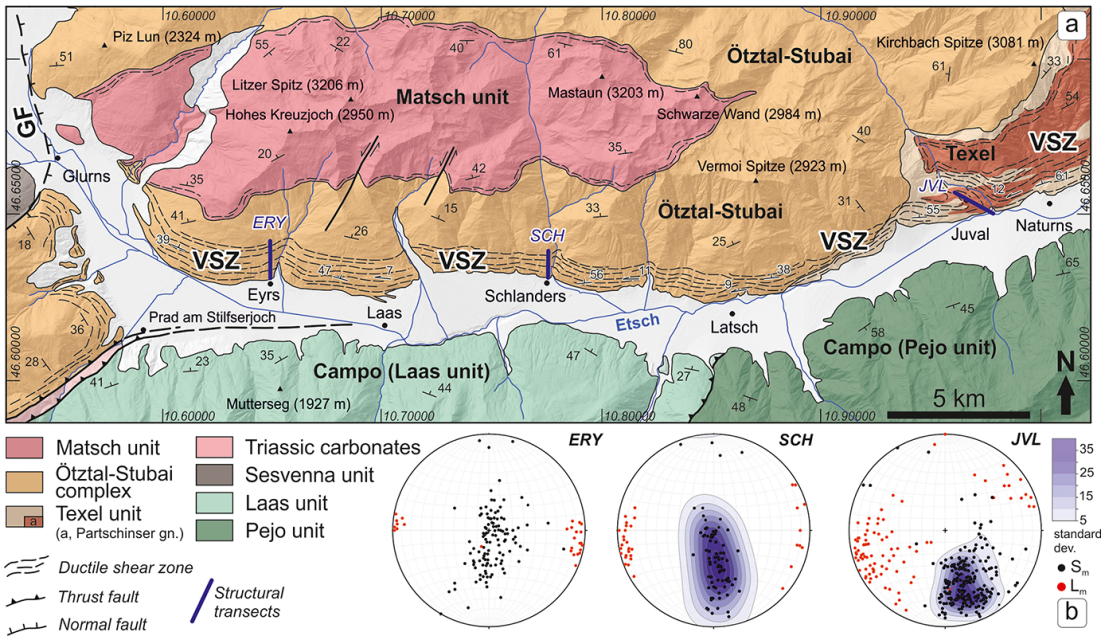

Figure 2. (a) Tectonic scheme of the Vinschgau Valley. The location of the studied transects (Eyrs, ERY; Schlanders, SCH; and Juval, JVL) is reported. **(b)** Structural data of Eyrs, Schlanders and Juval transects and equal area, lower-hemisphere stereographic projections of mylonitic foliation (S_m) and lineation (L_m); Kamb contours are represented as standard deviation. GF: Glurns Fault; VSZ: Vinschgau Shear Zone.

with temperatures that progressively decrease toward the northwest. Pressure estimates are substantially lacking. On the basis of newly formed mineralogical assemblages in pre-Alpine andesitic and andesitic/basaltic dikes intruding the Ötztal basement, Purtscheller and Rammlmair (1982) supposed a maximum pressure of about 0.5–0.6 Gpa, confirmed by recent data (Zanchetta et al., 2013). Additional P–T estimates have been proposed by Gregnanin and Valle (1995) for the Ötztal metasedimentary cover (550 °C and 1.0 Gpa) and by Tropper and Reichis (2003) for the SW part of the Ötztal basement (560 °C and 0.88 Gpa) close to the Schneeberg unit.

The westernmost portion of the VSZ is crosscut by the Glurns Fault (GF in Fig. 2), along which the Ötztal basement is in contact with the Sesvenna unit, mainly consisting of orthogneiss with a Variscan medium-grade metamorphic imprint and its Permian–Mesozoic sedimentary cover (Froitzheim et al., 1994, 1997).

3 Structural analysis

3.1 General description and methods

The entire VSZ has been individuated and followed in the field from Naturns (east) to Glurns (west) (Fig. 2). The maximum thickness is reached close to its western ends, at Eyrs, where it is estimated to be of about 600 m. To the east of Naturns (Fig. 2) the VSZ widens and branches out in several shear zones that wrap around the rigid body of the Partschinser orthogneiss of the Texel unit, as already noticed by Schmid and Haas (1989), which has given a Rb–Sr radiometric age of about 450 Ma for Partschinser orthogneiss (Zantedeschi, 1991). Here, in the Meran area, the VSZ is crosscut by most recent shear zones and faults (Bargossi et al., 2010).

Detailed field structural analyses and sampling of the VSZ were performed along three selected transects (Fig. 2) in the localities, from east to west, Juval, Schlanders and Eyrs. The three studied geological sections were chosen through field surveys and structural analyses. They are considered to be representative of the entire VSZ at different depths of exposure (shallowest conditions at Eyrs and deepest at Juval) and also offer the possibility of studying and sampling the shear zone in continuity, due to the good bedrock exposure. Each transect (Fig. 2) has been mapped at a 1 : 2000 scale, identifying the distribution of protomylonites, mylonites and ultramylonites following the classification by Simpson and De Paor (1993). Sampling sites were accurately selected on the basis of their representativity along the transects and the possibility they offered to perform microstructural and geochronological analyses.

3.1.1 The Juval transect

The easternmost transect is completely within the Texel unit. The cross-section extends southeast–northwest, from the bottom of the Vinschgau Valley to the Juval Castle. Here the road is entirely excavated in the bedrock, offering a continuous exposure of the entire shear zone. The bedrock mainly

consists of granitoid orthogneiss (Partschinser orthogneiss) showing different mylonitization degrees. This transect almost corresponds to the westernmost termination of the Texel unit (Fig. 2). Besides the Partschinser orthogneiss, the Texel unit here consists of garnet-, staurolite- and kyanite-bearing paragneisses that are also affected by mylonitization. They chiefly occur in the upper and central part of the transect, alternating with the orthogneiss. Some amphibolite boudins (Fig. 3d) are also exposed within the paragneiss along the road that leads to the Juval Castle. Paragneisses display a decrease in grain size with respect to the ones outside the VSZ, especially in the central part of the transect, where they can be classified as protomylonites. Analysis of the shear strain distribution highlights a symmetric increase, from rims to core, with ultramylonites and mylonites (Fig. 3) concentrated in the central part of the shear zone, whereas protomylonitic textures mainly occur close to both the structurally higher and lower margins. The mylonitic foliation is defined by the SPO (shape-preferred orientation; Passchier and Trouw, 2005) of biotite. The mylonitic lineation visible in outcrops mainly consists of elongated quartz aggregates and aligned biotite crystals (see Sect. 3.2 for details). Foliation dips towards the north-northwest, with mylonitic lineations that are nearly horizontal trending east-northeast–west-southwest (Fig. 2b). Moving toward the core of the shear zone, the clast–matrix ratio decreases, as does the size of K-feldspar porphyroclasts (Fig. 3). Ultramylonites appear as dark-gray bands within mylonites, a few centimeters up to 3–4 m in thickness (Fig. 3c). Quartz ribbons, a few millimeters in thickness and up to several decimeters in extension, frequently occur (Fig. 3e). Porphyroclasts are scarce within the ultramylonites, with a mean size not exceeding a few millimeters, whereas they commonly display a mean size of 20–30 mm outside the shear zone. Kinematic indicators represented by σ and δ clasts (Fig. 3b), antithetic bookshelves in K-feldspar porphyroclasts and SCC' fabric, invariably point to a top-to-W–WNW sense of shear.

3.1.2 The Schlanders transect

The Schlanders transect is located about 20 km to the west of the Juval section (Fig. 2). This section of the VSZ is entirely within the Ötztal polymetamorphic basement, here chiefly consisting of granitoid orthogneiss and minor two-mica paragneiss.

The upper portion of the structural transect extends outside the VSZ, where orthogneisses still preserve their metamorphic regional foliation of Variscan age (Schmid and Haas, 1989; Hoinkes et al., 1999; Thöni, 1999) gently dipping to the east. The cumulative shear strain distribution visible along this transect is symmetric, as was the case in the Juval section. Shear strain increases from the margins toward the core of the shear zone, with a decreasing grain size of both matrix and K-feldspar porphyroclasts. On the basis of the matrix–clast ratio (Simpson and De Paor, 1993), the orthogneiss is protomylonitic. Only towards the core of the shear zone do mylonitic bands occur, ranging in thickness from 10 to 50 cm. Ultramylonites, which are frequent along the Juval transect, occur here only as 2–10 cm thick bands, with a dark-gray color and an intense grain-size reduction (Fig. 3f). The mylonitic foliation dips to the north-northwest with a variable dip angle (Fig. 2b). Dip variations result from the occurrence of late-stage S-facing folds with E–W-trending fold axes that refold the mylonitic foliation. The lineation associated with top-to-W shearing is nearly subhorizontal or gently dipping to the west (Fig. 2b), identified in the field by elongate quartz aggregates and white micas.

3.1.3 The Eyrs transect

The Eyrs transect covers the western part of the exposed VSZ, close to the Schlinig Normal Fault and Glurns Fault (Figs. 1 and 2) that crosscut the shear zone. The exposed part of the VSZ is entirely developed again here within the Ötztal polymetamorphic basement, chiefly made of granitoid orthogneiss. Protomylonites and mylonites are preserved only along the upper margin of the shear zone, whereas the remaining part, from 1300 down to 900 m a.s.l. (meters above sea level), consists almost entirely of light-gray to whitish phyllonites (Fig. 3g). The phyllonites' protolith is hardly identifiable in the field, but the widespread occurrence (see Sect. 3.2) of K-feldspar suggests that mylonites and ultramylonites developed on pre-existing granitoid orthogneisses. Phyllonites are also exposed on the right side of the Vinschgau Valley (Fig. 2), northwest of Prad am Stilfserjoch. This part of the VSZ was probably the best known to past authors, and its fault rocks were previously known as the "Eyrs phyllites". The occurrence of dispersed carbonates (Fig. 3h) within the phyllonites led some authors to suppose the occurrence of Permian–Triassic carbonate sediments entrapped within the VSZ (Schmid and Haas, 1989).

Mylonitic foliation dips north-northwest with a variable dip angle due to the occurrence of S-facing folds, as described in the Schlanders transect (Fig. 2b). The mylonitic lineation, here mainly identified by iso-oriented sericite crystal on the foliation planes, is far less evident than in other sectors of the VSZ, but a WNW–ESE trend (Fig. 2b) is generally recognizable. The SPO of chlorite, white mica and quartz defines the mylonitic foliation. Extremely fine-grained quartz bands, a few millimeters thick, commonly occur (Fig. 3h). The light color of the phyllonites frequently turns into a brownish aspect (Fig. 3h). This is due to the occurrence of dispersed fine-grained carbonates (mainly calcite and Fe-dolomite; Fig. 3h) that likely originated from secondary fluids circulating along the shear zone. Secondary carbonates have also been found within orthogneiss-derived mylonites of the Juval transect.

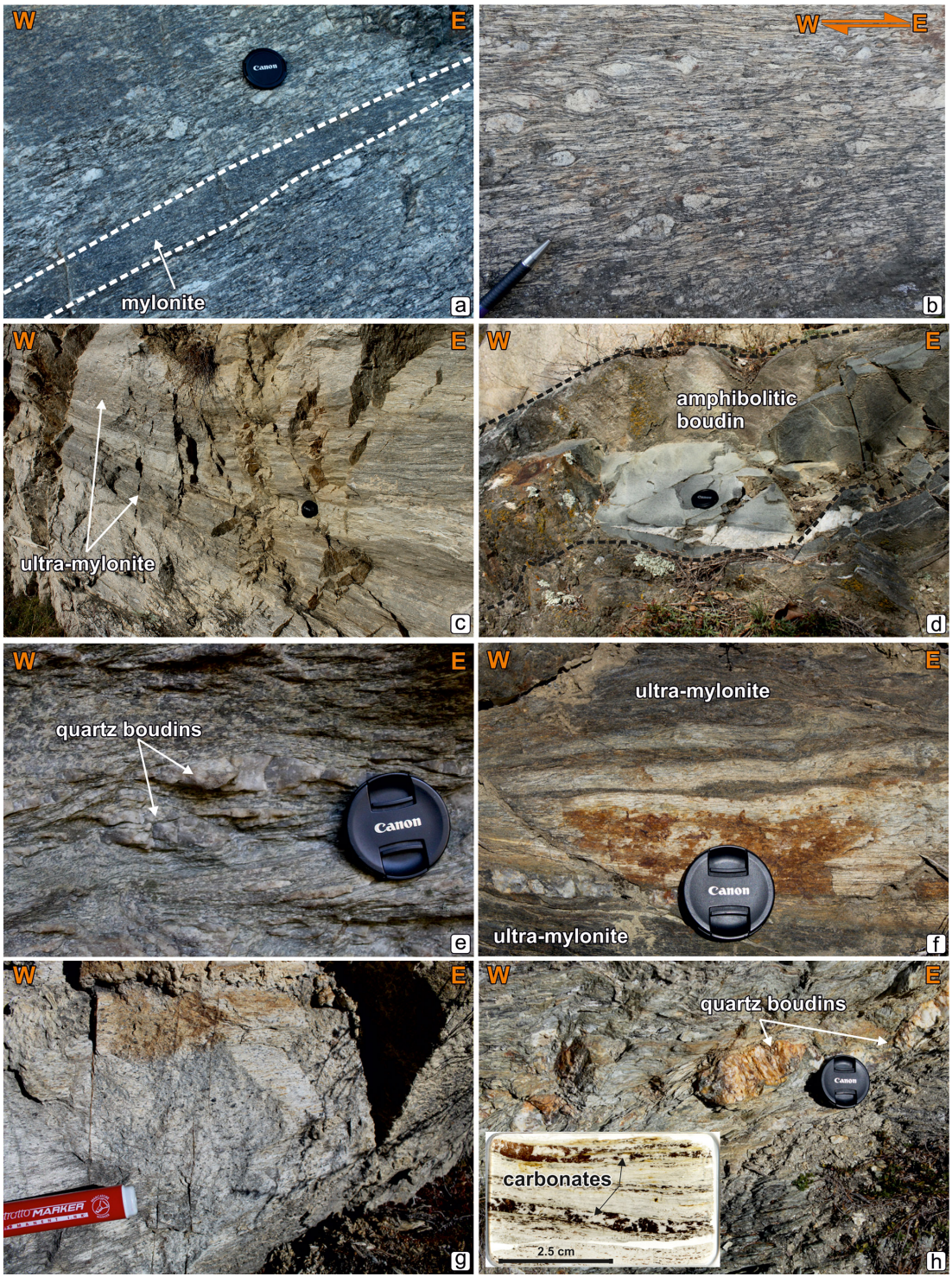

Figure 3. Field photographs of Juval, Schlanders and Eyrs outcrops. **(a)** Proto-mylonitic Partschinser orthogneiss with a mylonite band, recognizable from the darker color; reduced grain size; and rare presence of K-feldspar porphyroclasts (SW of Juval transect). **(b)** Proto-mylonite with asymmetric K-feldspar porphyroclasts and incipient SCC′ fabric showing a top-to-W sense of shear (south of Juval transect). **(c)** Mylonitic orthogneiss with ultra-mylonitic bands, recognizable from the dark-gray–black color; extremely reduced grain size; and quartz ribbon presence (southwest of Juval transect). **(d)** Mylonitic paragneiss with an amphibolitic boudin (central part of Juval transect). **(e)** Mylonitic orthogneiss with quartz boudins (east of Schlanders transect). **(f)** Mylonitic orthogneiss with black, fine-grained ultra-mylonitic bands (east of Schlanders transect). **(g)** Proto-mylonitic orthogneiss (northwest of Eyrs transect). **(h)** Phyllonite with quartz boudins (south of Eyrs transect). The image in the left corner shows the sample ERY-11, in which the calcite is clearly recognizable.

3.2 Microstructural analyses and kinematic vorticity of flow

Field structural analyses served as a basis for sampling of the different structural facies recognized along the studied VSZ transects. Samples were collected (Supplement Table S1) all along the three transects at regular distances in order to obtain a complete representation of the whole exposed shear zone.

Granitoid orthogneiss, the main protolith of the mylonites of the VSZ, does not represent the best opportunity for P–T estimates. The scarce changes in the equilibrium mineral assemblage and the variation in the mineral chemistry of representative phases (white mica, biotite, K-feldspar and plagioclase) under greenschist- and amphibolite-facies conditions make a precise estimate of pressure conditions difficult, and a qualitative, relative pressure determination can be estimated based on the Si content of white mica. Maximum temperature of mylonites could instead be determined by the stability of chlorite vs. biotite along the mylonitic foliation and the dominant quartz recrystallization mechanism (Stipp et al., 2002).

In the Juval transect poorly deformed orthogneiss and proto- and mylonitic orthogneiss consist of plagioclase, quartz, K-feldspar, white mica, biotite and chlorite. Rutile, apatite, titanite and zircon occur as accessory phases. The regional foliation is made by the SPO of $Bt_1 + Wm_1$ (Zantedeschi, 1991; Bargossi et al., 2010). Rare relicts of pre-mylonitic Bt have been reported on the easternmost termination of the Partschinser orthogneiss body, outside the VSZ (Bargossi et al., 2010). The mylonitic foliation is defined by the SPO of $Wm_1 + Bt_1$, with white mica more abundant than biotite. Chlorite has only rarely been observed, mainly as an initial destabilization of biotite along rims of the Bt_2 grains. Bt_2 and Wm_2 overprinting the main foliation are observed in some samples (Fig. 4b).

In the poorly deformed orthogneiss, quartz is recrystallized mainly via the bulging (BLG; Passchier and Trouw, 2005) recrystallization mechanism (Fig. 4a). Within proto- and mylonitic orthogneiss the dominant mechanism is subgrain rotation (SGR; Passchier and Trouw, 2005; Fig. 4b) recrystallization. A well-developed SCC' fabric (Fig. 5), together with various groups of mica fish (group 1 to 5 of Passchier and Trouw, 2005; group 5 in Fig. 4c) and asymmetric K-feldspar porphyroclasts (Fig. 4d), points to a top-to-W shear sense, as already observed in the field.

In the Schlanders transect, chlorite substitutes biotite along the mylonitic foliation, pointing to lower temperatures during shearing than in the Juval section. The syn-mylonitic foliation is defined here by the SPO of $Ms_{III} + Chl$. The complete mineralogy of mylonites consists of plagioclase, quartz, K-feldspar, white mica, chlorite and rare relicts of biotite. Apatite, rutile and zircon are usually present as accessory phases. Mylonites along the Schlanders transect are often seen to grade into phyllonites, with a strong decrease in grain size and a progressive increase in white mica with respect to chlorite. Within phyllonites, K-feldspar has been preserved only as relicts 1–3 mm in size, with white mica becoming the major mineral phase. The occurrence of fine-grained white mica domains characterizes most of the phyllonites, often affected by a weak crenulation (Fig. 4e) in response to E–W-trending, S-facing folds, as previously described. Together with the increase in white mica abundance, carbonates also increase. They occur as calcite and Fe-calcite crystals, reaching about 5 % of the volume of the whole rock. Quartz in mylonites displays textures compatible with SGR recrystallization, whereas BLG is the only recrystallization mechanism observed in phyllonites.

In the Eyrs transect, the westernmost and, following Schmid and Haas (1989), the shallowest transect of the VSZ, phyllonites completely substitute mylonites. The whole of the shear zone consists of extremely fine-grained light-gray to whitish phyllonites. Phyllosilicate domains reach up to 60 % of the rock volume, with white mica as the major mineral phase. The abundance of calcite increases, reaching up to 10 % in several outcrops. Calcite and Fe-calcite crystal show type 1 and type 2 deformation twinning (Ferrill et al., 2004; Fig. 4f). Quartz recrystallizes via BLG; no relicts of SGR and GBM (grain boundary migration; Passchier and Trouw, 2005). P textures have been observed in samples from the Eyrs transect. SCC' fabric, foliation fish, mica fish (group 3 and 4) and K-feldspar porphyroclasts occur as kinematic indicators, pointing to a top-to-W sense of shear.

To define the type of flow within the VSZ, kinematic vorticity analyses were performed on five samples (JVL-16, JVL-12, JVL-11, JVL-6, JVL-14) collected along the Juval transect oriented perpendicular to the shear zone boundaries. The vorticity analysis was carried out on Juval samples, as they are suitable for vorticity estimates. Unfortunately, Schlanders and Eyrs mylonites are unsuitable for the application of any of the methods of vorticity estimates due to the lack of fabrics which allow application of vorticity estimate methods (e.g., shear bands fabric, porphyroclasts or oblique foliation in quartz).

The analyses were performed on thin sections cut perpendicular to foliation and parallel to lineation (i.e., the XZ plane of the finite-strain ellipsoid) using the C′ shear band method (Kurz and Northrup, 2008), considering the mean value of the orientation of the synthetic shear bands following the interpretation of Gillam et al. (2013). Polar histograms used to derive the angle (2ν) between the apophyses A_1 and A_2 are reported in Fig. 5.

The C′ shear band method reveals W_m ranging from 0.64 up to 0.87, corresponding to a variation in simple shear component of 46 %–68 %, with the kinematic vorticity decreasing towards the core of the shear zone.

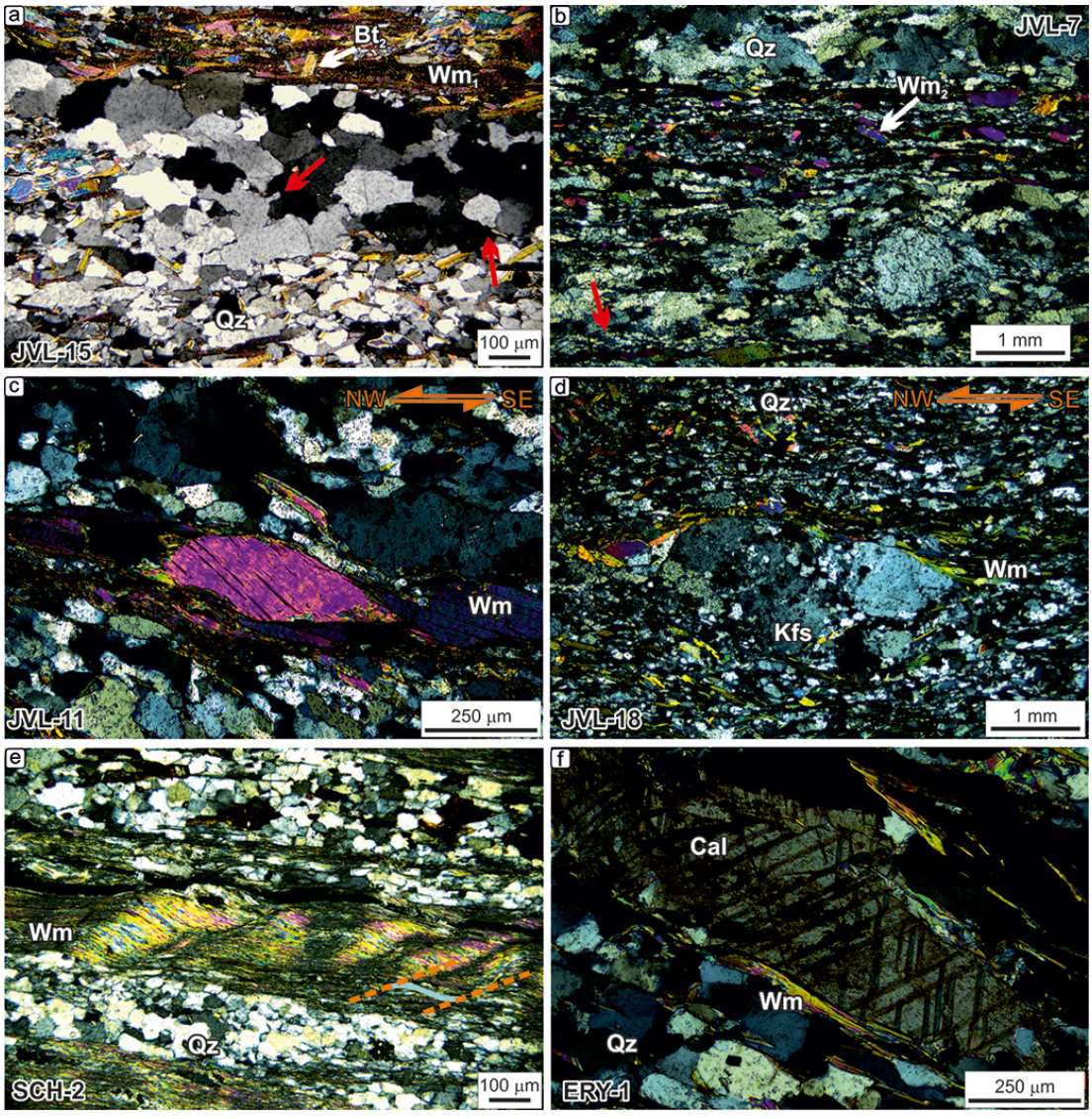

Figure 4. Representative photomicrographs from the VSZ, crossed polars. **(a)** Quartz recrystallized via bulging recrystallization mechanism (red arrows) in poorly deformed Partschinser orthogneiss. The white arrow points at Bt_2. **(b)** Quartz recrystallized via subgrain rotation recrystallization mechanism (red arrows) and static white mica (Wm_2, white arrow) growing on the main foliation (Wm_1) at a high angle. Close-up of **(c)** group 5 mica fish according to the classification of Passchier and Trouw (2005) and **(d)** asymmetric K-feldspar porphyroclasts. **(e)** A well-developed crenulation cleavage in phyllonite and **(f)** deformation twinning in calcite.

4 Petrochronology

4.1 Mineral chemistry

Electron microprobe analyses (EMPAs) were carried out using a JEOL 8200 Super Probe EMP at the Dipartimento di Scienze della Terra "A. Desio", Università degli Studi di Milano. Quantitative chemical analyses were performed on carbon-coated petrographic thin sections. Data acquisition was performed using an accelerating voltage of 15 kV, a beam current of 5 nA and a spot size of 1 µm. Natural silicates and oxides were used as standards. White mica and biotite analyses were recalculated as atoms per formula unit (apfu) based on 11 oxygens.

Quantitative chemical analyses were performed on a non-mylonitic orthogneiss sample (JVL-15), on mylonitic orthogneiss samples (JVL-1, JVL-7, JVL-13, SCH-4) and on a phyllonite sample (ERY-11), with a total of about 100 points. Chemical analyses are reported in Fig. 6 and Supplement Table S2. Both the first and second generations of micas were analyzed; the microstructurally older white mica and biotite generation forming the main mylonitic foliation (hereafter Wm_1 and Bt_1) and the following static white mica and biotite

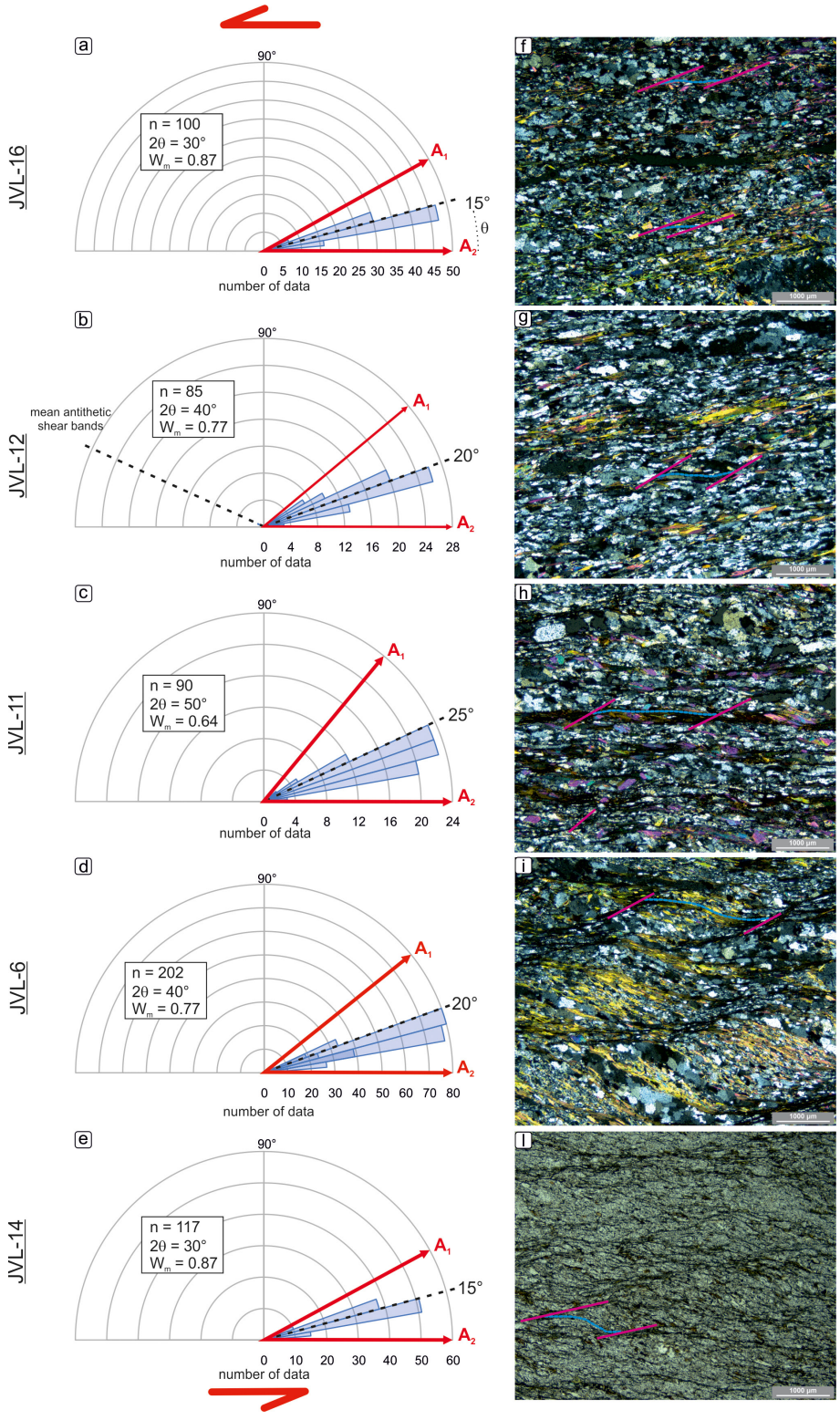

Figure 5. Vorticity estimates through SC′ **(a–e)** and relative SC′ fabric **(f–l)**. Polar histograms used to derive the angle θ and to calculate kinematic vorticity with the SC′ method (Kurz and Northrup, 2008) for samples JVL-16 **(a)**, JVL-12 **(b)**, JVL-11 **(c)**, JVL-6 **(d)** and JVL-14 **(e)**. C′ shear bands are highlighted with violet lines and the main foliation *S* with dotted blue lines **(f–l)**.

generation overprinting the preceding one (hereafter Wm_2 and Bt_2).

4.1.1 White mica

Considering all six samples, some compositional variations around the muscovite–celadonite join can be observed, with Si ranging between 3.1 and 3.4 apfu and Al ranging between 2.17 and 2.71 apfu (Fig. 6a). White mica in ERY-11 is characterized by the highest Al/Si ratios, while the other samples show gradually decreasing Al/Si ratios, with JVL-7 and SCH-4 being the lowest (Fig. 6a). White mica in JVL-1, JVL-7, JVL-13 and JVL-15 samples is characterized by a negative correlation between Al and Si content (Fig. 6a), ranging from Si content between 3.14 and 3.35 apfu and Al content between 2.17 and 2.55 apfu. White mica from sample JVL-7 displays a compositional cluster characterized by high Si content (3.30–3.34 apfu) and low Al content (2.17–2.22 apfu), whereas white mica from sample JVL-15 shows an opposite cluster with low Si (3.17–3.20 apfu) and high Al (2.46–2.49 apfu) content (Fig. 6a). No variations in Al and Si contents have been detected between first- and second-generation white mica (Ms1 and Ms2, respectively).

The Na / (Na+K) ratio (Fig. 6b; Guidotti and Sassi, 1998) of white mica in sample ERY-11 is higher (0.09–0.13) than in sample SCH-4 (0.01–0.02) and in samples JVL-1, JVL-7, JVL-13 and JVL-15 (0.02–0.07). No variations in the Na / (Na+K) ratio were observed on Wm_1 and Wm_2. White mica in JVL-1, JVL-7, JVL-13 and JVL-15 samples shows a homogenous distribution of the Na / (Na+K) ratio (0.02–0.07), with Si content ranging between 3.14 and 3.34 apfu (Fig. 6b).

4.1.2 Biotite

Analyses were performed on biotite from five samples since it was absent from sample SCH-4. In the sample ERY-11 the X_{Mg} ratio ranges between 0.54 and 0.56 (Fig. 6c–d), whereas X_{Mg} of the other samples shows a cluster at lower values (0.34–0.46). As in the case of white mica analyses, no significant chemical variations have been observed between the two biotite generations (Bt_1 and Bt_2).

The Si content of biotite in sample ERY-11 is homogenous, while in samples JVL-1, JVL-7, JVL-13 and JVL-15 it shows a cluster characterized by Si content between 2.74 and 2.83 apfu (Fig. 6c). The Ti content in biotite from samples JVL-1, JVL-7, JVL-13 and JVL-15 is clustered at values between 0.08 and 0.17 apfu (Fig. 6d), apart from a biotite-2 from sample JVL-7, which shows a remarkably lower value (0.01 apfu), like sample ERY-11 (0.001–0.006 apfu).

The K content (Supplement Table S2) reveals that in sample ERY-11, all the spot analyses yielded low, sub-stoichiometric K in Bt_1 and Bt_2. These values, very close to the detection limit (ca. 0.006–0.010 apfu), pertain to chlorite, as also supported by the matching element sums below 96 % for these analyses (Supplement Table S2). Biotite from samples JVL-1, JVL-7, JVL-13 and JVL-15 is characterized by K content of 0.93–1.00 apfu, except for a biotite-2 from sample JVL-7, which again shows low K content (0.02 apfu). As in the case of sample ERY-11, the low K content and the element sums (ca. 89 %; Supplement Table S2) confirm the presence of chlorite in the sample.

4.2 $^{40}Ar/^{39}Ar$ geochronological constraints on the VSZ activity

White mica and biotite used for $^{40}Ar/^{39}Ar$ geochronology were obtained from rock samples: JVL-1, JVL-7, JVL-13, JVL-15, SCH-1, SCH-4, SCH-5, ERY-3, ERY-8 and ERY-11. The mineral separation was performed at the Dipartimento di Scienze dell'Ambiente e della Terra, Università degli Studi di Milano – Bicocca. Rock samples were crushed and sieved, then Wm_1 and Bt_1 in the 125–500 µm fraction were enriched by magnetic techniques and subsequently purified by hand-picking. Mica separates were cleaned and rinsed in pure deionized water by a two-step procedure in ultrasonic baths.

Mica samples were irradiated in the McMaster University Research Reactor (Hamilton, CA), carefully avoiding Cd shielding. $^{40}Ar/^{39}Ar$ step-heating analyses were carried out using a double-vacuum resistance furnace attached to a Nu Instruments Noblesse rare-gas mass spectrometer at the Dipartimento di Scienze dell'Ambiente e della Terra, Università degli Studi di Milano – Bicocca. The irradiation monitor was a McClure Mountain hornblende (MMhb) with an assumed age of 523.98 ± 0.12 Ma (Schoene and Bowring, 2006). The decay constants were those of Steiger and Jäger (1977). Step-heating experiments were conducted following the analytical protocols of Montemagni and Villa (2021). This approach evaluates and integrates the information deriving from the age spectra, the correlation diagram (i.e., Ca/K vs. age) and the differential release plot (i.e., T vs. differential release). The obtained ages are therefore isochemical ages; the steps used for the age calculation are those with the lowest and homogeneous Ca/K ratios, which correspond to the highest release of ^{39}Ar and percentage of ^{39}Ar. All $^{40}Ar/^{39}Ar$ data are reported in Supplement Table S3.

4.2.1 The Juval transect

The age spectrum, the correlation diagram (Ca/K vs. age) and the differential release plots (DRPs) for white mica display similar features (Fig. 7). The ^{39}Ar degassing peaks in the DRP (occurring at temperatures ranging between 1080–1300 K) correspond to the flat part of the spectrum and the lowest Ca/K values, as imposed by white mica stoichiometry, which should be Ca-free. The heating steps showing high Ca/K and high Cl/K ratios (derived from the measured $^{37}Ar/^{39}Ar$ and $^{38}Ar/^{39}Ar$) monitor the degassing of Ca-rich alteration phases and have been disregarded in the age calculation. At higher temperatures pertaining to white

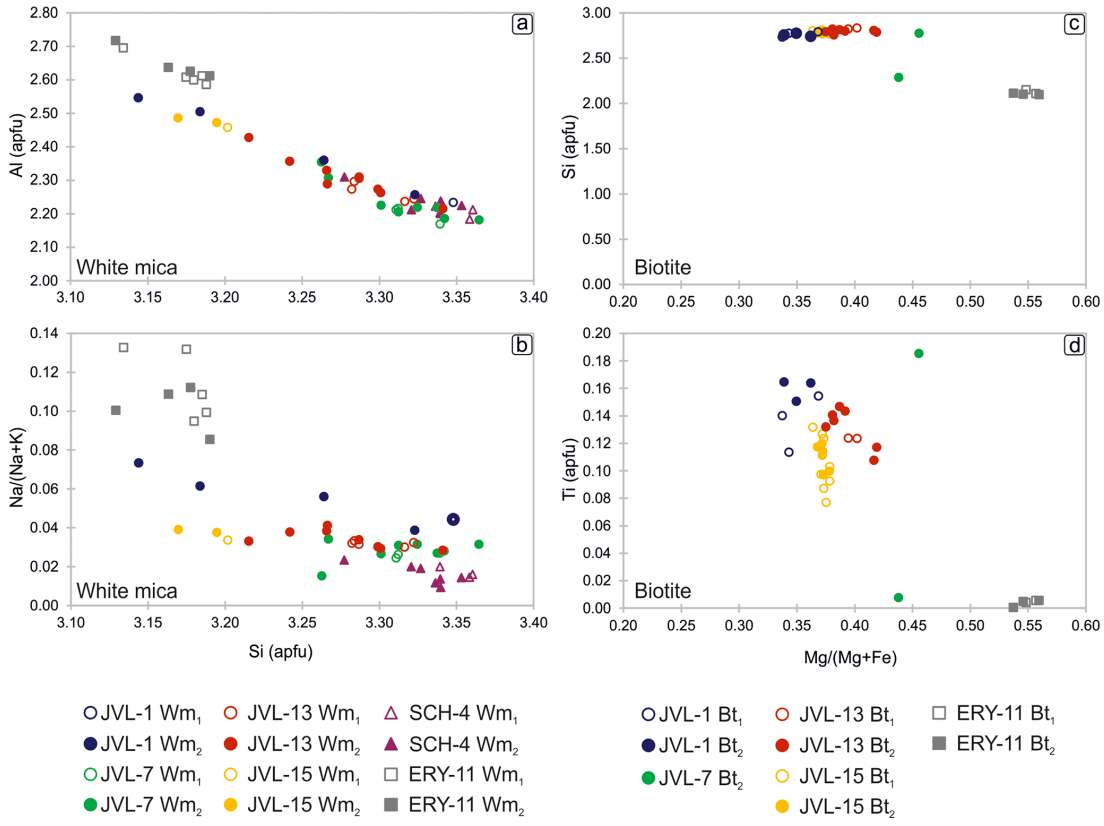

Figure 6. EPMA (electron microprobe analysis) results showing compositional variation in white mica **(a–b)** and biotite **(c–d)**.

mica or biotite degassing, the Ca/K and Cl/K reach a minimum. Biotite gas release patterns behave likewise, whereby the ^{39}Ar release peak occurs at a lower temperature (ca. 960 K; Fig. 7c, f, i, n, as extensively documented for Himalayan mylonites by Montemagni and Villa (2021) and Alpine ones in Montemagni and Zanchetta (2022). The age of mylonitic foliation on biotite, constraining the VSZ activity, is 87.40 ± 1.06 Ma (JVL-1; Fig. 7a), 80.36 ± 0.46 Ma (JVL-7; Fig. 7d), 84.75 ± 0.40 Ma (JVL-13; Fig. 7g) and 92.28 ± 0.34 Ma (JVL-15; Fig. 7l).

4.2.2 The Schlanders transect

The ^{39}Ar release patterns of the three white mica samples SCH-1, SCH-4 and SCH-5 (Fig. 8) are different from those of Juval. All three Schlanders samples show a bimodal ^{39}Ar peak pattern: one release around 940 K, typical of chlorite (see Montemagni and Villa, 2021), and one around 1050–1150 K, typical of white mica. In SCH-4 and SCH-5 the white mica release peak corresponds to the lowest Ca/K ratios, i.e., the flat part of the spectra. In SCH-1 the white mica release peak is not very evident, but the three steps between 1080 and 1200 K correspond to low and homogenous Ca/K ratios, coherent with the Ar release in SCH-4 and SCH-5. The age of mylonitic foliation has been constrained at 95.35 ± 1.50 Ma (SCH-1; Fig. 8a), 89.37 ± 0.24 Ma (SCH-4; Fig. 8d) and 97.86 ± 0.24 Ma (SCH-5; Fig. 8g).

4.2.3 The Eyrs transect

The phyllonites (ERY-3 and ERY-8) contain dispersed carbonates, evidence of massive fluid circulation (Fig. 3h). Moreover, due to the lower strain rate and/or lower temperature, the micas did not fully recrystallize during the Cretaceous faulting and give meaningless mixed ages with substantial Ar inheritance, and white mica ages are geologically meaningless (Fig. 9a–d). The age of mylonitic foliation has been constrained to be 92.58 ± 1.56 Ma (ERY-11; Fig. 9g).

5 Discussion

5.1 Kinematic and chronological evolution of the VSZ

Although the Vinschgau Shear Zone (VSZ) is one of the largest thrust-sense shear zones exposed in the Alps, no age constraints existed on the shearing activity of this huge intra-Austroalpine thrust, with its Late Cretaceous age only inferred on the basis of indirect evidence (Schmid and Haas, 1989) and a single Rb–Sr whole-rock age of a deformed pegmatite (Thöni, 1986). Our ^{40}Ar/^{39}Ar data are the first attempt

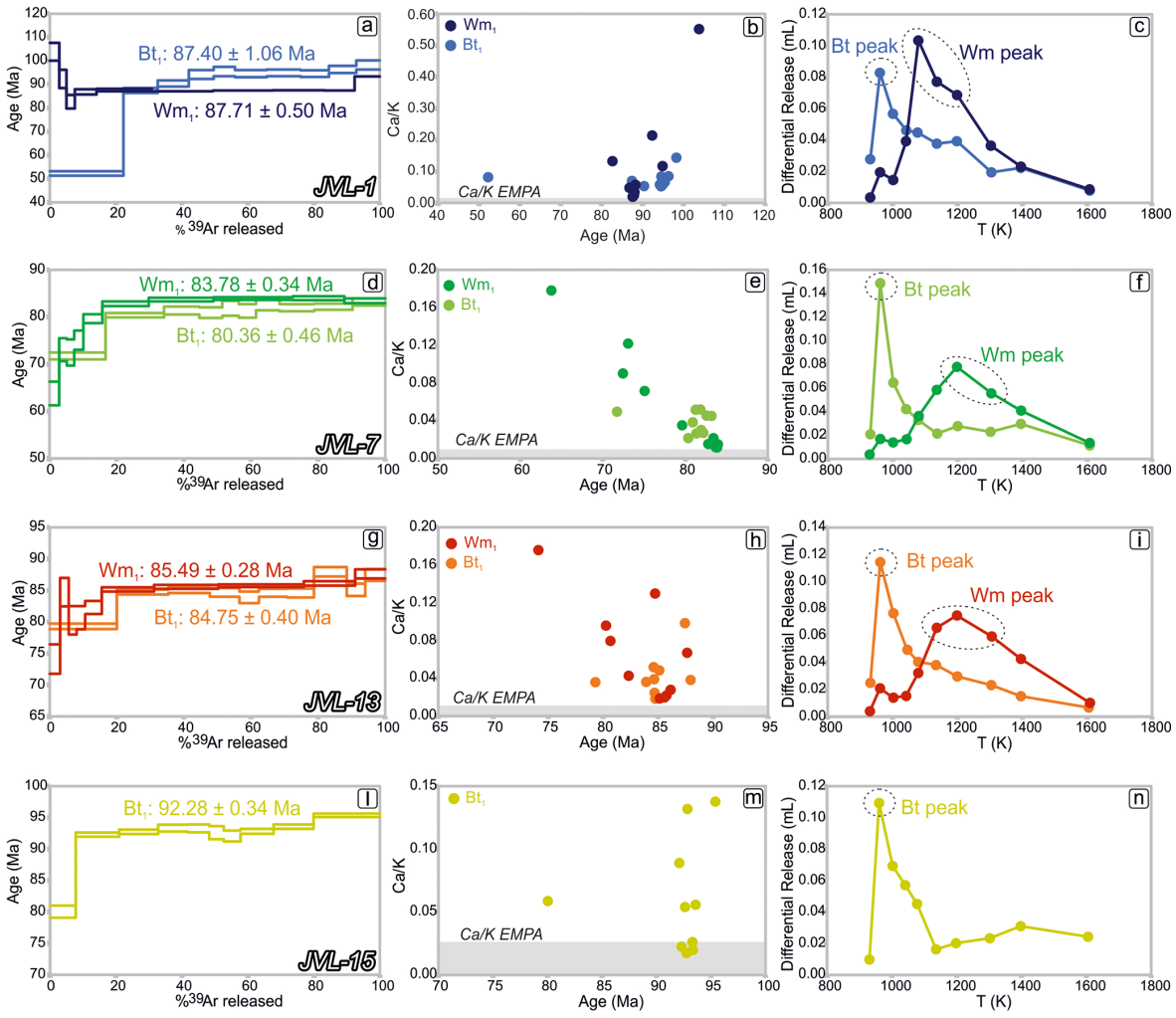

Figure 7. $^{40}Ar/^{39}Ar$ age spectra, Ca/K vs. age diagrams and differential release plots for Juval samples JVL-1 **(a–c)**, JVL-7 **(d–f)**, JVL-13 **(g–i)** and JVL-15 **(l–n)**. The dotted circles in the T vs. differential release plots **(c, f, i, n)** indicate the degassing steps selected for the age calculation.

to constrain the time interval of activity of the VSZ, combining geochronological results obtained across the shear zone and along its dip direction.

The evolution of shear zones has been deeply investigated in terms of spatial variation, especially concerning their length and thickness (Hull, 1988; Mitra, 1992; Means, 1995; Vitale and Mazzoli, 2008, 2010; Fossen, 2016; Fossen and Cavalcante, 2017). This effort was aimed at defining the parameters that may influence the evolution of one type of shear zone with respect to another one. If the growth in length of a shear zone is essentially due to linkage of different branches forming a composite system of shear zones (Fossen and Cavalcante, 2017), the growth in thickness may be influenced by different mechanisms. Four ideal models of shear zone evolution have been proposed and discriminated based on shear strain gradient, kinematic vorticity, and plane or triaxial strain (Vitale and Mazzoli, 2008; Fossen and Cavalcante, 2017). Processes of strain hardening or strain softening promote the thickening and the thinning of the shear zone, respectively type 1 or type 2 models. In the type 1 model, the deformation concentrates in the margins of the shear zone, leaving the inner portion inactive. In contrast, in the type 2 model the deformation shifts and concentrates in the inner portion of the shear zone as strain accumulates, leaving the margins inactive. In addition, the type 3 model is related to a strain-weakening process, even if its active thickness remains constant with time. The type 4 model expands in thickness, but, unlike type 1, all the thickness remains active through time. According to the several models proposed for shear zone evolution (Fossen and Cavalcante, 2017, with references), the VSZ followed a type 2 evolutionary model, with increasing cumulative shear strain from margins to the core of the shear zone (Fig. 10). This pattern of shear strain distribution is demonstrated for the VSZ by the occurrence

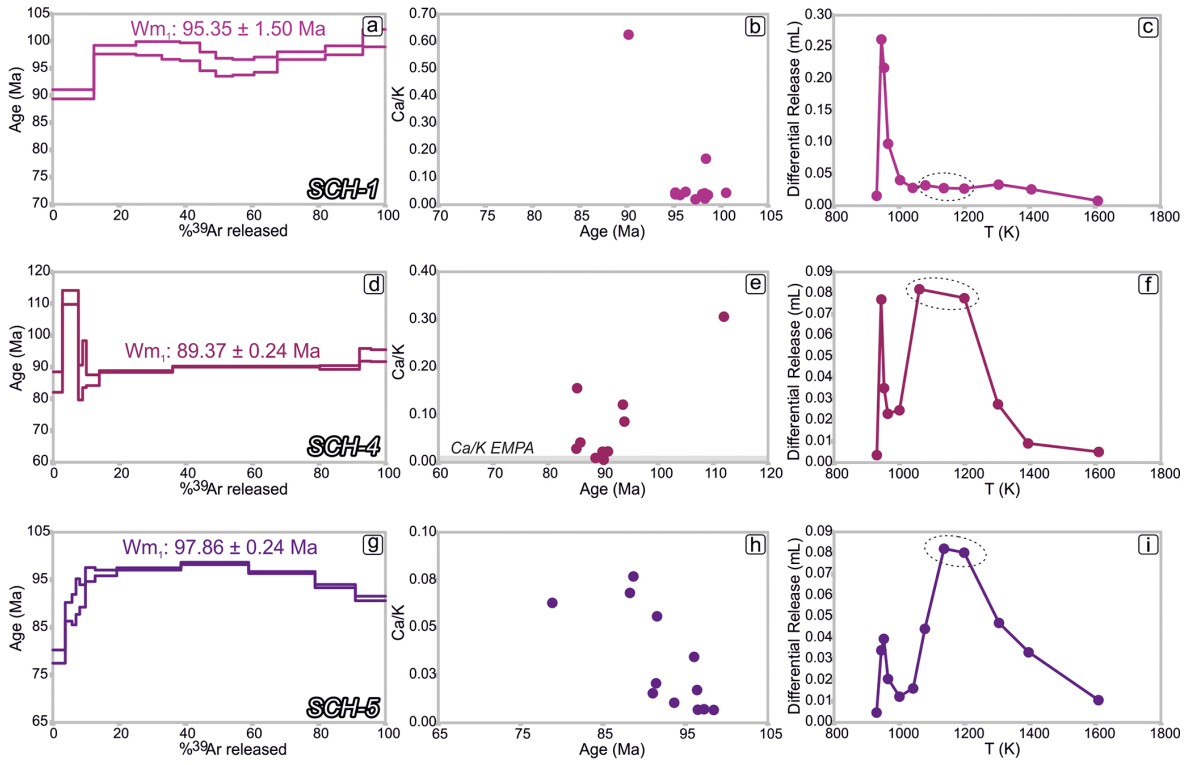

Figure 8. ^{40}Ar/^{39}Ar age spectra, Ca/K vs. age diagrams and differential release plots for Schlanders samples SCH-1 **(a–c)**, SCH-4 **(d–f)** and SCH-5 **(g–i)**. The dotted circles in the T vs. differential release plots **(c, f, i)** indicate the degassing steps selected for the age calculation.

of ultramylonites at the core of the Juval transect (Fig. 10), whereas protomylonites derived from the Partschinser orthogneiss are preserved only at the margins. The kinematic vorticity of flow follows the same symmetric distribution, with W_m that increases from the rims to the core (ca. 0.64 at the margins and ca. 0.87 at the core; Fig. 10). The patterns displayed by the shear strain point to a strain-softening behavior of the shear zone (e.g., Vitale and Mazzoli, 2008). At the microscale, the processes that may cause strain softening are (i) recrystallization during shearing, especially when associated with the subgrain rotation recrystallization mechanism (Passchier and Trouw, 2005), which leads to formation of new grains with lower dislocation density that results in a deformation at lower differential stress, and (ii) shear band fabric formation (Fig. 5), as shear bands imply local grain-size reduction, a mechanism which is invoked in low to medium mylonitization to promote strain weakening (Fossen and Cavalcante, 2017, and references therein). Lattice preferred orientation (Fig. 4) may also weaken the rheology as recrystallized or newly formed minerals, mainly micas and quartz, have intracrystalline slip planes aligned in the shear direction, resulting in favorable motion of dislocations with continuous dynamic recrystallization also at low differential stress (Passchier and Trouw, 2005, with references).

The VSZ deepens from west to east, as suggested by previous workers (Schmid and Haas, 1989) and confirmed by the present data, with white mica–chlorite phyllonites overprinting white mica–biotite mylonites in the western part of the shear zone. Broadly, the ^{40}Ar/^{39}Ar ages rejuvenate from west to east, opposite to the transport direction and consequent exhumation of the Austroalpine units in the hanging wall. This age pattern points to younger ages of shearing in the east (i.e., Juval area), where deeper portions were still being deformed (Fig. 11), while in the west the shear zone was already at shallow crustal depths.

Beyond the deformational path of the VSZ, which clearly follows a strain-softening type 2 shear-zone-evolution model, the novelty of our work is the integration of microstructural and kinematic analyses with age profiling of the shear zone along its transport direction, along its depth and across its strike (Fig. 11). The obtained age pattern allows the reconstruction of a time-resolved evolution of the shear zone during its progressive activity and exhumation.

The ^{40}Ar/^{39}Ar ages recorded by micas in the Schlanders and Juval transects reveal a clear younging trend from the margin to the inner zone of the shear zone (Figs. 7, 8 and 11). This trend of younging mica ages is paralleled by increasing cumulative shear strain and decreasing simple shear component (Fig. 11). The correlation between ages and deformation suggests a progressive migration of deformation towards the inner portion of the VSZ, with the margin becoming inactive (as testified by older mylonite ages $\geq$ 97 Ma), while defor-

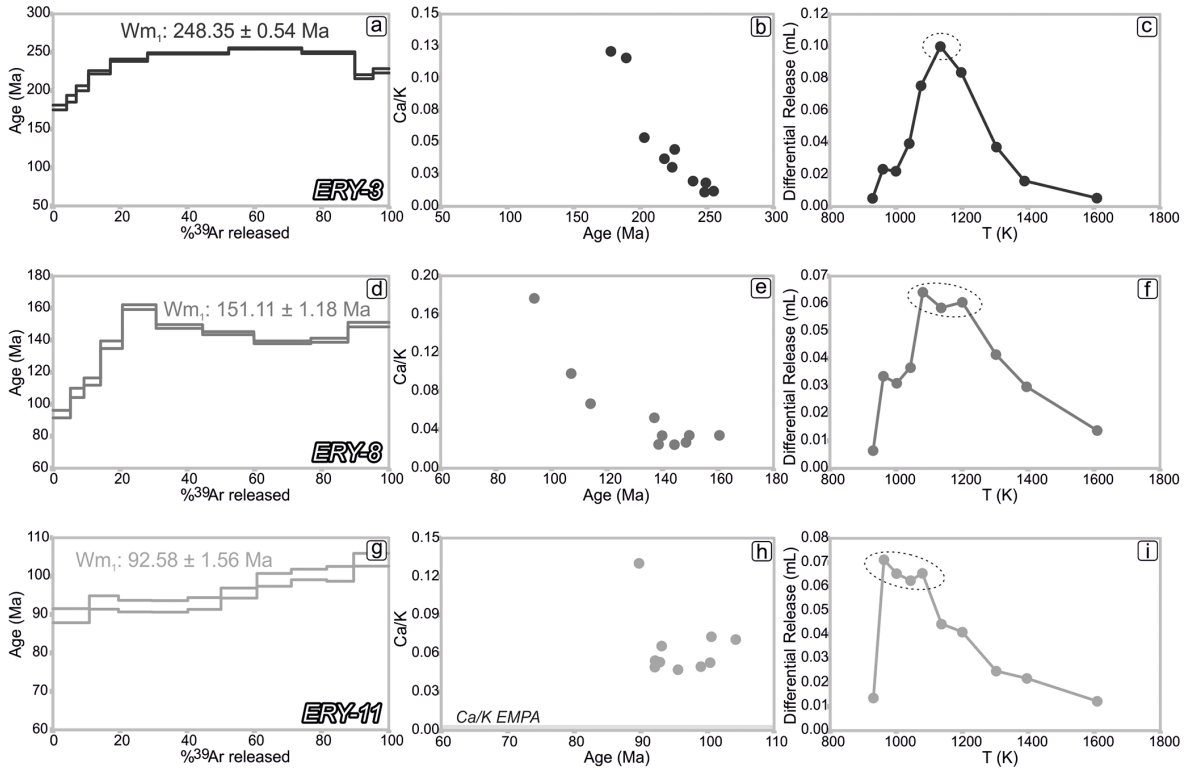

Figure 9. $^{40}Ar/^{39}Ar$ age spectra, Ca/K vs. age diagrams and differential release plots for Eyrs samples ERY-3 **(a–c)**, ERY-8 **(d–f)** and ERY-11 **(g–i)**. The dotted circles in the *T* vs. differential release plots **(c, f, i)** indicate the degassing steps selected for the age calculation.

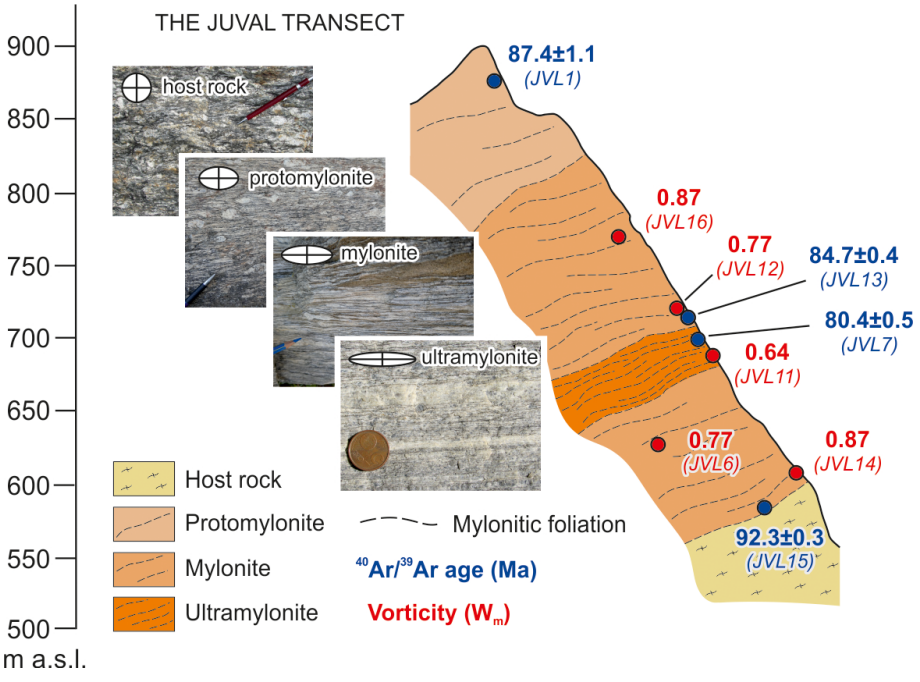

Figure 10. Schematic cross-section of Juval transect showing the occurrence of protomylonites, mylonites and ultramylonites developed along the strain gradient from the rim to the core of the shear zone, with $^{40}Ar/^{39}Ar$ age (in blue) and kinematic vorticity number (in red). Samples not in the profile have been projected along the strike of the mylonitic foliation.

mation concentrates in the middle of the shear zone, where micas show younger ages down to 80 Ma.

5.2 The VSZ in an evolving orogenic wedge

The evolution of the Eo-Alpine orogenic wedge of the eastern Alps is generally related to the closure of the Meliata Ocean, located in an intra-Austroalpine position (e.g., Schmid et al., 2004) or separating the former Austroalpine and Southalpine domain (e.g., Neubauer et al., 2000). Other interpretations consider instead the possibility that the entire Austroalpine orogenic wedge formed in the Late Cretaceous in a pre-collisional setting (Zanchetta et al., 2012, 2015).

Irrespective of the geodynamic scenario of the Eo-Alpine orogen in the eastern Alps, the VSZ acted as a crustal-scale shear zone promoting nappe stacking and exhumation within an orogenic wedge chiefly made of continent-derived tectonic units. The ages of shearing along the VSZ indicate that the shear zone was already active at 97 Ma (Figs. 7, 8 and 11), at least 7–8 Myr before the pressure peak recorded by the Texel eclogites and the amphibolitic peak in the Schneeberg unit. The ages of the VSZ in the Schlanders transects overlap with published/available ages related to the peak of Alpine metamorphism in the Ötztal basement, suggesting that thrusting within the Austroalpine domain started where units in the hanging wall of the VSZ had already reached (Ötztal) or were close to the metamorphic peak (Texel and Schneeberg units). This age overlap between shearing and metamorphic peak is explained by a rapid exhumation of these HP rocks via thrusting in the Eo-Alpine orogenic wedge. Handy et al. (2010) argued that the Eo-Alpine orogen, in the time span 118–84 Ma, was subjected to intracontinental subduction and basement nappe stacking, whose evidence is the E–W-trending belt of Late Cretaceous, HP rocks of the Koralpe–Wölz nappe complex (Schmid et al., 2004; Thöni et al., 2008), to which the Texel and Schneeberg units belong. The exhumation of these HP rocks was both westward and northward (Handy et al., 2010).

The WSW-directed Late Cretaceous thrusting (Eisbacher and Brandner, 1996; Ratschbacher, 1986; Schmid and Haas, 1989; Viola et al., 2003; Handy et al., 2010) and consequent nappe stacking under pressure-dominated, amphibolite- to greenschist-facies conditions are unusual if compared to major NNW-directed direction of transport for other sectors of the Alps. This scenario has been explained through a complex microplate configuration at 94 Ma, which necessarily invokes the faster eastward accommodation of the Iberia microplate with respect to the Adria microplate, also moving eastward with respect to Europe, but at lower rates (Handy et al., 2010).

The age of the pressure metamorphic peak within HP units has been reported to be between 95 and 89 Ma (Thöni, 2002; Habler et al., 2006; Miller et al., 2005; Thöni et al., 2008; Janák et al., 2009; Zanchetta et al., 2013), with partially overlapping ages related to their rapid exhumation (e.g., Fügenschuh et al., 1997; Sölva et al., 2005).

As the Texel and the Ötztal units are now in tectonic contact at the eastern termination of the VSZ, at least 20 km of vertical exhumation of the Texel unit should have been accommodated along the VSZ, considering the difference in peak metamorphic pressure recorded by the two units (Fig. 11a): 1.2–1.4 GPa for the Texel unit (Habler et al., 2006) and 0.5–0.6 GPa for the Ötztal basement (Purtscheller and Rammlmair, 1982). Considering a lithostatic pressure gradient of $0.03\,\mathrm{GPa\,km^{-1}}$ and a consequent difference in terms of pressure of 0.6 GPa between the Ötztal and the Texel unit, such vertical displacement corresponds to a minimum of about 40 km along the shear zone, taking into account a dip of about 30°, which is typical of a thrust-sense shear zone active through crustal depths controlling the exhumation of high-grade units in their hanging wall (e.g., Jamieson et al., 2004). The amount of E–W shortening within the Austroalpine basement nappes has been estimated to be $\geq$ 100–150 km (Manatschal and Bernoulli, 1999; Schmid et al., 2020).

The VSZ yields ages in the range of 80 Ma (the youngest age at the inner portion of the Juval transect) to 97 Ma (the oldest age in the Schlander area), almost coeval with the peak metamorphic age in the Ötztal and Texel units at ca. 85–90 Ma (Zanchetta et al., 2013; Fig. 11). Hence, we argue that the VSZ has been active at least for 17 Ma, promoting the rapid exhumation of the Texel eclogite in the Late Cretaceous. Syn-shearing exhumation of the Texel and Schneeberg units continued at least up to 76 Ma, as testified by the age of greenschist-facies mylonites along shear zones within these two units (Sölva et al., 2005). This scenario was also depicted by Handy et al. (2010), who suggested a rapid exhumation of the Koralpe–Wölz units during the Cenomanian–Santonian (ca. 94–84 Ma), when the Gosau Group (syn- to post-orogenic clastic sediments sometimes deposited in intra-orogenic extensional basins) sealed thrusts in the Austroalpine basement and in the northern Calcareous Alps.

Exhumation models for crystalline rocks have been extensively proposed; modeled; and tested for Himalayan orogen, where the exhumation of the metamorphic core of the belt was a matter of debate in the literature (e.g., Montomoli et al., 2015; Carosi et al., 2018; Montemagni, 2020). Regardless of the specific model, the scientific community agrees that exhumation in the Himalayas has been driven by two opposite shear zones bounding the crystalline core: a normal-sense at its top and a thrust-sense shear zone at its bottom, respectively (e.g., Godin et al., 2006; Montomoli et al., 2013, for reviews). Based on structural and geochronological data, a similar model was also proposed for the eclogite type locality in the Saualpe region (Wiesinger et al., 2006). A recent study (Schulz and Krause, 2021) documented the younger age in amphibolite-grade footwall units underlying the eclogite-bearing unit.

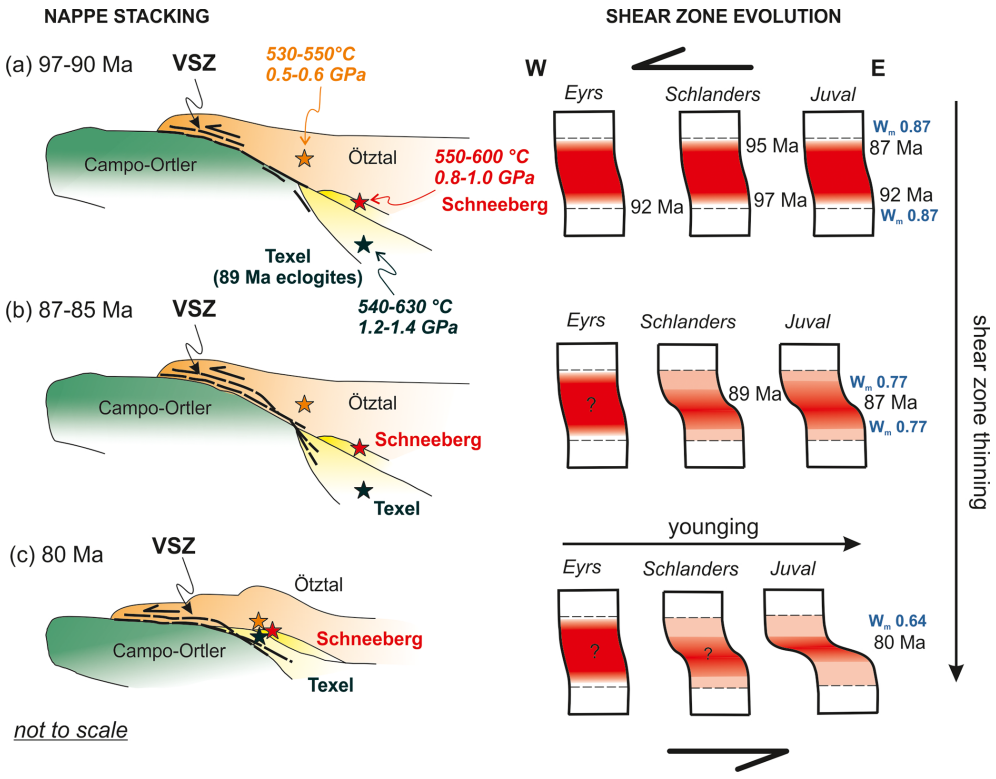

Figure 11. Evolution of the Vinschgau Shear Zone in the orogenic Eo-Alpine wedge during the Late Cretaceous. Activation of the VSZ **(a)** in the time span 97–90 Ma affecting the Ötzal unit. **(b)** In the period 87–85 Ma the VSZ also affected the Texel unit and **(c)** during the late stage of shearing exhumed the Texel and Schneeberg units, bringing them into tectonic contact with the Ötzal complex. In **(a)** the P–T conditions for the Ötzal, Texel and Schneeberg units are reported. The dashed lines represent the thickness and length of the shear zone through time. The evolution of the VSZ in the studied transects in term of ages, cumulative shear strain and kinematic vorticity is also shown.

From this perspective, we argue that the VSZ played a key role in the exhumation of HP rocks in the eastern Alps, and we can speculate that the units containing HP rocks have been exhumed by a (not necessarily coeval) shearing of a thrust-sense shear zone at the base and a normal-sense shear zone at the top of the orogenic wedge, i.e., above the Ötztal–Stubai complex. Considering the jump in the metamorphic grade and age of metamorphism between the underlying Eo-Alpine Ötztal–Stubai complex (garnet amphibolites facies) and the quartz-phyllites (ca. 350 °C of peak temperature; Lünsdorf et al., 2012) with a pre-Permian metamorphic age (Rockenschaub et al., 2003) of the Steinach nappe, the shear zone at the base of this nappe could be a valuable candidate for the normal-sense shear zone that together with the VSZ controlled the exhumation of the high-pressure Ötztal–Texel–Schneeberg complex.

Besides the geodynamic interpretation, the presented data indicate that the VSZ had a long-lasting evolution of at least 17 Myr. The minimum accommodated displacement of ca. 40 km implies a displacement rate of 2–2.5 mm yr^{-1}, which is significantly higher than the values reported in Vitale and Mazzoli (2008) of 0.10 mm yr^{-1} for the thinning shear zone (type 2). The accommodated displacement of the VSZ is coherent with slip rate values of ca. 10 mm yr^{-1} reported by Stübner et al. (2013) for an intra-basement normal-sense shear zone in the Pamir plateau. The exhumation continued rapidly, as suggested by thermochronological data in the eastern Ötztal–Stubai complex unit, where cooling below 60 °C at 60 Ma has been reported (Fügenschuh et al., 1997).

6 Conclusions

The VSZ is one of the prominent intra-basement thrust-sense shear zones developed in the Alps, promoting the exhumation of HP rocks within the Eo-Alpine orogenic wedge.

Our approach fully constrains its kinematic and temporal evolution:

i. Cumulative shear strain and kinematic vorticity values reveal an evolution compatible with a type 2 thinning shear zone.

ii. ^{40}Ar/^{39}Ar geochronology defines the shearing activity to be between 97 and 80 Ma, resulting in a long-lasting deformation history.

iii. The novelty of our work is the combination of microstructural and kinematic analyses with age profiling of the shear zone both along its transport direction and across its strike.

Data availability. Our original data (EMPA analyses on micas and Ar–Ar data) are provided in the Supplement with public access (Tables S2 and S3).

Supplement. The supplement related to this article is available online at: https://doi.org/10.5194/se-14-551-2023-supplement.

Author contributions. SZ, AZ and CM designed the study, and CM and MR carried it out. The paper was prepared by CM and SZ and revised by AZ with the contribution of all co-authors. All authors participated in fieldwork and in the various scientific discussions.

Competing interests. The contact author has declared that none of the authors has any competing interests.

Disclaimer. Publisher's note: Copernicus Publications remains neutral with regard to jurisdictional claims in published maps and institutional affiliations.

Acknowledgements. We warmly thank the reviewers Franz Neubauer and Paolo Conti for their careful and significant comments that improved the paper and Yang Chu for the editorial handling of the manuscript. We are also grateful to Hannah Pomella for corrections of the German toponyms and discussion about the Vinschgau geology that helped us to clarify some aspects. We thank Andrea Risplendente (Università degli Studi di Milano) for his support during the electron microprobe analyses and Valentina Barberini (Università degli Studi di Milano – Bicocca) for the maintenance of the mass spectrometer.

Financial support. This research has been supported by the Ministero dell'Università e della Ricerca (grant no. 2021-NAZ-0299, CUP: J33C22000170001) and the Provincia Autonoma di Bolzano – Alto Adige (grant no. 2022-NOECO-0131 PROGETTO MALLES).

Review statement. This paper was edited by Yang Chu and reviewed by Paolo Conti and Franz Neubauer.

References

Bargossi, G. M., Bove, G., Cucato, M., Gregnanin, A., Morelli, C., Moretti, A., Poli, S., Zanchetta, S., and Zanchi, A.: Note illustrative della Carta Geologica d'Italia – Merano foglio 013, Servizio Geologica d'Italia – ISPRA, 2010.

Brunel, M.: Quartz fabrics in shear-zone mylonites: evidence for a major imprint due to late strain increments, Tectonophysics, 64, T33–T44, 1980.

Caby, R., Pêcher, A., and Le Fort, P.: Le grand chevauchement central himalayen: Nouvelles données sur le métamorphisme inverse à la base de la Dalle du Tibet, Rev. Géol. Dynam. Géograph. Phys., 24, 89–100, 1983.

Carosi, R., Montomoli, C., and Iaccarino, S.: 20 years of geological mapping of the metamorphic core across Central and Eastern Himalayas, Earth-Sci. Rev., 177, 124–138, 2018.

Conti, P.: La Falda Austroalpina dell'Ortles e l'evoluzione tettonica delle Dolomiti dell'Engadina (Svizzera-Italia), Memorie Descrittive della Carta Geologica D'Italia, Servizio Geologico d'Italia, Roma, 53, 102 pp., 1997.

D'Adda, P. and Zanchetta, S.: Geological-structural map of the Orobic and Porcile thrust junction, central Southern Alps (N Italy), J. Maps, 11, 25–38, 2015.

Eisbacher, G. H. and Brandner, R.: Superposed fold-thrust structures and high-angle faults, Northwestern Calcareous Alps, Austria, Eclogae Geol. Helv., 89, 553–571, 1996.

Ferrill, D. A., Morris, A. P., Evans, M. A., Burkhard, M., Groshong Jr., R. H., and Onasch, C. M.: Calcite twin morphology: a low-temperature deformation geothermometer, J. Struct. Geol., 26, 1521–1529, 2004.

Fossen, H.: Structural geology, Cambridge University Press, ISBN 9781107057647, 2016.

Fossen, H. and Cavalcante, G. C. G.: Shear zones – A review, Earth Sci. Rev., 171, 434–455, https://doi.org/10.1016/j.earscirev.2017.05.002, 2017.

Froitzheim, N., Schmid, S. M., and Conti, P.: Repeated change from crustal shortening to orogen-parallel extension in the Austroalpine units of Graubünden, Eclogae Geol. Helv., 87, 559–612, 1994.

Froitzheim, N., Conti, P., and van Daalen, M.: Late Cretaceous, synorogenic, low-angle normal faulting along the Schlinig fault (Switzerland, Italy, Austria) and its significance for the tectonics of the Eastern Alps, Tectonophysics, 280, 267–293, 1997.

Fügenschuh, B., Seward, D., Mancktelow, N., and Fumasoli, M.: Exhumation in a convergent orogen: the western Tauern window, Terra Nova, 9, 213–217, 1997.

Gillam, B. G., Little, T. A., Smith, E., and Toy, V. G.: Extensional shear band development on the outer margin of the Alpine mylonite zone, Tatare Stream, Southern Alps, New Zealand, J. Struct. Geol., 54, 1–20, https://doi.org/10.1016/j.jsg.2013.06.010, 2013.

Godin, L., Grujic, D., Law, R. D., and Searle, M. P.: Channel flow, ductile extrusion and exhumation in continental collision zones: an introduction, in: Channel flow, ductile extrusion and exhumation in continental collision zones, edited by: Law, R. D., Searle, M. P., and Godin, L., Geol. Soc. London Spec. Pub., 268, 1–23, 2006.

Gregnanin, A. and Valle, M.: Deformation and metamorphism in the Austroalpine Ötztal-Stubai complex (part II): Early Alpine

evolution in basement and cover, Boll. Soc. Geol. It., 114, 393–409, 1995.

Guidotti, C. V. and Sassi, F. P.: Miscellaneous isomorphous substitutions in Na-K white micas: a review, with special emphasis to metamorphic micas, Rend. Lincei. Sci. Fis. Nat., 9, 57–78, 1998.

Habler, G., Thöni, M., and Sölva, H.: Tracing the high pressure stage in the polymetamorphic Texel Complex (Austroalpine basement unit, Eastern Alps): P-T-t-d constraints, Miner. Petrol., 88, 269–296, 2006.

Habler, G., Thöni, M., and Grasemann, B.: Cretaceous metamorphism in the Austroalpine Matsch Unit (Eastern Alps): the interrelation between deformation and chemical equilibration processes, Miner. Petrol., 97, 149–171, 2009.

Handy, M., Schmid, S., Bousquet, R., Kissling, E., and Bernoulli, D.: Reconciling plate-tectonic reconstructions of Alpine Tethys with the geological–geophysical record of spreading and subduction in the Alps, Earth-Sci. Rev., 102, 121–158, 2010.

Hanmer, S., Bowring, S., van Breemen, O., and Parrish, R.: Great Slave Lake shear zone, NW Canada: mylonitic record of Early Proterozoic continental convergence, collision and indentation, J. Struct. Geol., 14, 757–773, 1992.

Heim, A.: Geologie der Schweiz, Band II, Die Schweizer Alpen, Tauchnitz, Leipzig, 1018 pp., 1922.

Hoinkes, G., Koller, F., Rantitsch, G., Dachs, E., Höck, V., Neubauer, F., and Schuster, R.: Alpine metamorphism of the Eastern Alps, Schweiz. Miner. Petrogr., 79, 155–181, 1999.

Hull, J.: Thickness-displacement relationships for deformation zone, J. Struct. Geol., 10, 431–435, https://doi.org/10.1016/0191-8141(88)90020-X, 1988.

Jamieson, R. A., Beaumont, C., Medvedev, S., and Nguyen, M. H.: Crustal channel flows: 2. Numerical models with implications for metamorphism in the Himalayan-Tibetan orogen, J. Geophys. Res.-Sol. Ea., 109, B06407, https://doi.org/10.1029/2003JB002811, 2004.

Janák, M., Cornell, D., Froitzheim, N., De Hoog, J. C. M., Broska, I., Vrabec, M., and Hurai, V.: Eclogite hosting metapelites from the Pohorje Mountains (Eastern Alps): P-T evolution, zircon geochronology and tectonic implications, Eur. J. Mineral., 21, 1191–1212, 2009.

Klug, L. and Froitzheim, N.: Reuniting the Ötztal Nappe: the tectonic evolution of the Schneeberg Complex, Int. J. Earth Sci., 111, 525–542, 2022.

Koltai, G., Cheng, H., and Spötl, C.: Palaeoclimate significance of speleothems in crystalline rocks: a test case from the Late Glacial and early Holocene (Vinschgau, northern Italy), Clim. Past, 14, 369–381, https://doi.org/10.5194/cp-14-369-2018, 2018.

Konzett, J. and Hoinkes, G.: Paragonite-hornblende assemblages and their petrological significance: an example from the Austroalpine Schneeberg Complex, Southern Tyrol, Italy, J. Metamorph. Geol., 14, 85–101, 1996.

Krenn, K., Kurz, W., Fritz, H., and Hoinkes, G.: Eoalpine tectonics of the Eastern Alps: implications from the evolution of monometamorphic Austroalpine units (Schneeberg and Radenthein Complex), Swiss J. Geosci., 104, 471–491, 2011.

Kurz, G. A. and Northrup, C. J.: Structural analysis of mylonitic rocks in the Cougar Creek Complex, Oregon–Idaho using the porphyroclast hyperbolic distribution method, and potential use of SC′-type extensional shear bands as quantitative vorticity indicators, J. Struct. Geol., 30, 1005–1012, https://doi.org/10.1016/j.jsg.2008.04.003, 2008.

Law, R. D., Stahr, D. W., Francsis, M. K., Ashley, K. T., Grasemann, B., and Ahmad, T.: Deformation temperatures and flow vorticities near the base of the Greater Himalayan Series, Sutlej valley and Shimla Klippe, NW India, J. Struct. Geol., 54, 21–53, https://doi.org/10.1016/j.jsg.2013.05.009, 2013.

Lünsdorf, N. K., Dunkl, I., Schmidt, B. C., Rantitsch, G., and Eynatten H.: The thermal history of the Steinach Nappe (Eastern Alps) during extension along the Brenner Normal Fault system indicated by organic maturation and zircon (U-Th)/He thermochronology, Austr. J. Earth. Sci., 105, 17–25, 2012.

Manatschal, G. and Bernoulli, D.: Architecture and tectonic evolution of nonvolcanic margins: present-day Galicia and ancient Adria, Tectonics, 18, 1099–1119, 1999.

Mancktelow, N. S.: The Simplon Line: a major displacement zone in the western Lepontine Alps, Eclogae Geol. Helv., 78, 73–96, 1985.

Means, W. D.: Shear zones and rock history, Tectonophysics, 247, 157–160, https://doi.org/10.1016/0040-1951(95)98214-H, 1995.

Miller, C., Mundil, R., Thöni, M., and Konzett, J.: Refining the timing of eclogite facies metamorphism: a geochemical, petrological, Sm–Nd and U–Pb case study from the Pohorje Mountain, Slovenia (Eastern Alps), Contrib. Mineral. Petr., 150, 70–84, 2005.

Mitra, G.: Deformation of granitic basement rocks along fault zones at shallow to intermediate crustal levels, in: Structural Geology of Fold and Thrust Belts, edited by: Mitra, S. and Fisher, G. W., Johns Hopkins University Press, Baltimore, MD, 123–144, 1992.

Montemagni, C.: Geochronology and Kinematics of Crustal Scale Shear Zones in the Himalayan Collisional Belt, PhD thesis, Università degli Studi di Milano – Bicocca, https://hdl.handle.net/10281/269277 (last access: 18 May 2023), 2020.

Montemagni, C. and Villa, I. M.: Geochronology of Himalayan shear zones: unravelling the timing of thrusting from structurally complex fault rocks, J. Geol. Soc. London, 178, 1–13, https://doi.org/10.1144/jgs2020-235, 2021.

Montemagni, C. and Zanchetta, S.: Constraining kinematic and temporal evolution of a normal-sense shear zone: Insights into the Simplon Shear Zone (Western Alps), J. Struct. Geol., 156, 104557, https://doi.org/10.1016/j.jsg.2022.104557, 2022.

Montomoli, C., Iaccarino, S., Carosi, R., Langone, A., and Visonà, D.: Tectonometamorphic discontinuities within the Greater Himalayan Sequence in Western Nepal (Central Himalaya): Insights on the exhumation of crystalline rocks, Tectonophysics, 608, 1349–1370, 2013.

Montomoli, C., Carosi, R., and Iaccarino, S.: Tectonometamorphic discontinuities in the Greater Himalayan Sequence: a local or a regional feature?, in: Tectonics of the Himalaya, edited by: Mukherjee S., van der Beek, P., and Mukherjee, P. K., Geol. Soc. London Spec. Publ., 412, 21–41, 2015.

Neubauer, F., Genser, J., and Handler, R.: The Eastern Alps: Result of a two stage collision process, Mitt. Österr. Geol. Ges., 92, 117–134, 2000.

Oriolo, S., Oyhantçabal, P., Wemmer, K., Heidelbach, F., Pfander, J., Basei, M. A. S., Hueck, M., Hannich, F., Sperner, B., and Siegesmund, S.: Shear zone evolution and timing of deformation in the Neoproterozoic transpressional

Dom Feliciano Belt, Uruguay, J. Struct. Geol., 92, 59–78, https://doi.org/10.1016/j.jsg.2016.09.010, 2016.

Oriolo, S., Wemmer, K., Oyhantçabal, P., Fossen, H., Schulz, B., and Siegesmund, S.: Geochronology of shear zones – a review, Earth Sci. Rev., 185, 665–683, https://doi.org/10.1016/j.earscirev.2018.07.007, 2018.

Passchier, C. W. and Trouw, R. A. J.: Microtectonics, Springer Verlag, Berlin, ISBN 978-3-540-64003-5, https://doi.org/10.1007/3-540-29359-0, 2005.

Petroccia, A., Carosi, R., Montomoli, C., Iaccarino, S., and Brovarone, A. V.: Deformation and temperature variation along thrust-sense shear zones in the hinterland-foreland transition zone of collisional settings: A case study from the Barbagia Thrust (Sardinia, Italy), J. Struct. Geol., 161, 104640, https://doi.org/10.1016/j.jsg.2022.104640, 2022.

Poli, S.: Reaction spaces and P–T paths: from the amphibole eclogite to the greenschist facies in the Austroalpine domain (Oetztal Complex), Contrib. Mineral. Petr., 106, 399–416, 1991.

Pomella, H., Flöss, D., Speckbacher, R., Tropper, P., and Fügenschuh, B.: The western end of the Eoalpine High-Pressure Belt (Texel unit, South Tyrol/Italy), Terra Nova, 28, 60–69, https://doi.org/10.1111/ter.12191, 2016.

Purtscheller, F. and Rammlmair, D.: Alpine metamorphism of diabase dikes in the Ötztal-Stubai metamorphic complex, Tschermaks Mineral. Petrogr. Mitt., 29, 205–221, 1982.

Ratschbacher, L.: Kinematics of Austro-Alpine cover nappes; changing translation path due to transpression, Tectonophysics, 125, 335–356, 1986.

Ratschbacher, L., Neubauer, F., Frisch, W., Schmid, S. M., and Neugebauer, J.: Extension in compressional orogenic belts: The eastern Alps, Geology, 17, 404–407, 1989.

Rockenschaub, M. (Ed.), Kolenprat, B., and Frank, W.: Geochronologische Daten aus dem Brennergebiet: Steinacher Decke, Brennermesozoikum, Ötz-Stubai-Kristallin, Innsbrucker Quarzphyllitkomplex, Tarntaler Mesozoikum, in: R Arbeitstagung 2003 der Geologischen Bundesanstalt, Geologische Kartehblätter 148 Brenner, 175 Sterzing, 117–124, Geologische Bundesanstalt, Wien, 2003

Rosenberg, C. L., Schneider, S., Scharf, A., Bertrand, A., Hammerschmidt, K., Rabaute, A., and Brun, J. P.: Relating collisional kinematics to exhumation processes in the Eastern Alps, Earth Sci. Rev. 176, 311–344, https://doi.org/10.1016/j.earscirev.2017.10.013, 2018.

Schmid, S. M. and Haas, R.: Transition from near-surface thrusting to intrabasement decollement, Schlinig Thrust, Eastern Alps, Tectonics, 8, 697–718, https://doi.org/10.1029/TC008i004p00697, 1989.

Schmid, S. M., Zingg, A., and Handy, M.: The kinematics of movements along the Insubric Line and the emplacement of the Ivrea Zone, Tectonophysics, 135, 47–66, 1987.

Schmid, S. M., Aebli, H. R., Heller, F., Zingg, A., Coward, M. P., Dietrich, D., and Park, R. G.: The role of the Periadriatic Line in the tectonic evolution of the Alps Alpine Tectonics, Geol. Soc. London Spec. Pub., 45, 153–171, 1989.

Schmid, S. M., Fügenschuh, B., Kissling, E., and Schuster, R.: Tectonic map and overall architecture of the Alpine orogen, Eclogae Geol. Helv., 97, 93–117, 2004.

Schoene, B. and Bowring, S. A.: U–Pb systematics of the McClure Mountain syenite: thermochronological constraints on the age of the $^{40}Ar/^{39}Ar$ standard MMhb, Contrib. Mineral. Petr., 151, 615–630, https://doi.org/10.1007/s00410-006-0077-4, 2006.

Schulz, B. and Krause, J.: Electron probe petrochronology of polymetamorphic garnet micaschists in the lower nappe units of the Austroalpine Saualpe basement (Carinthia, Austria), Z. Dtsc. Ges. Geowiss., 172, 19–46, https://doi.org/10.1127/zdgg/2021/0247, 2021.

Searle, M. P., Law, R. D., Godin, L., Larson, K. P., Streule, M. J., Cottle, J. M., and Jessup, M. J.: Defining the Himalayan Main Central Thrust in Nepal, J. Geol. Soc. London, 165, 523–534, 2008.

Simpson, C. and De Paor, D. G.: Strain and kinematic analysis in general shear zones, J. Struct. Geol., 15, 1–20, 1993.

Sölva, H., Grasemann, B., Thöni, M., Thiede, R., and Habler, G.: The Schneeberg normal fault zone: normal faulting associated with Cretaceous SE-directed extrusion in the Eastern Alps (Italy/Austria), Tectonophysics, 410, 143–166, 2005.

Spitz, A. and Dyrenfurth, G.: Monographie der Engadiner Dolomiten zwischen Schuls, Scanfs und der Stilfserjoch, Beitr. Geol. Karte Schweiz (NF), XLIV, Lief, 1914.

Staub, R.: Geologische Probleme zwischen Engadin und Ortler, Denkschr. Schweiz. Naturf. Ges., 72, 1–115, 1937.

Steiger, R. and Jäger, E.: Subcommission on geochronology: convention on the use of decay constants in geo-and cosmochronology, Earth Planet. Sc. Lett., 36, 359–362, 1977.

Stipp, M., Stunitz, H., Heilbronner, R., and Schmid, S. M.: The eastern Tonale fault zone: A natural laboratory for crystal plastic deformation over a temperature range from 250 to 700 °C, J. Struct. Geol., 24, 1861–1884, 2002.

Stübner, K., Ratschbacher, L., Weise, C., Chow, J., Hofmann, J., Khan, J., and Project TIPAGE members: The giant Shakhdara migmatitic gneiss dome, Pamir, India-Asia collision zone: 2. Timing of dome formation, Tectonics, 32, 1404–1431, 2013.

Thöni, M.: Distribution of pre-Alpine and Alpine metamorphism of the southern Ötztal Mass and the Scarl Unit, based on K/Ar age determinations, Mitt. Österr. Geol. Ges., 71, 139–165, 1980.

Thöni, M.: Degree and Evolution of the Alpine Metamorphism in the Austroalpine Unit W of the Hohe Tauern in the light of K/Ar and Rb/Sr Age Determinations on Micas, Jahrbuch der Geologischen Bundesanstalt, 124, 111174, 1981.

Thöni, M.: The Rb-Sr thin slab isochron Method-an Unreliable Geochronologic Method for Dating Geologic Events in Polymetamorphic Terrains?: Evidence from the Austroalpine Basement Nappe, the Eastern Alps, Mem. Soc. Geol., 38, 283–352, 1986.

Thöni, M.: A review of geochronological data from the Eastern Alps, Schweiz. Mineral. Petrogr. Mitt., 79, 209–230, 1999.

Thöni, M.: Sm–Nd isotope systematics in garnet from different lithologies (Eastern Alps): age results, and an evaluation of potential problems for garnet Sm–Nd chronometry, Chem. Geol., 185, 255–281, https://doi.org/10.1016/S0009-2541(02)00419-9, 2002.

Thöni, M., Miller, C., Blichert-Toft, J., Whitehouse, M. J., Konzett, J., and Zanetti, A.: Timing of high-pressure metamorphism and exhumation of the eclogite-type locality (Klupperbrunn-Prickler Halt, south-eastern Austria): constraints from the correlation of the Sm-Nd, Lu-Hf, U-Pb and Rb-Sr isotopic systems, J. Metamorph. Geol., 26, 561–581, 2008.

Tropper, P. and Reiches, A.: Garnet zoning as a window into the metamorphic evolution of a crystalline complex: the northern and central Austroalpine Ötztal-Complex as a polymetamorphic example, Mitt. Österr. Geol. Ges., 94, 27–53, 2003.

Vitale, S. and Mazzoli, S.: Heterogeneous shear zone evolution: the role of shear strain hardening/softening, J. Struct. Geol., 30, 1383–1395, https://doi.org/10.1016/j.jsg.2008.07.006, 2008.

Vitale, S. and Mazzoli, S.: Strain analysis of heterogeneous ductile shear zones based on the attitudes of planar markers, J. Struct. Geol., 32, 321–329, 2010.

Xypolias, P.: Vorticity analysis in shear zones: a review of methods and applications, J. Struct. Geol., 32, 2072–2092, https://doi.org/10.1016/j.jsg.2010.08.009, 2010.

Xypolias, P. and Koukouvelas, I. K.: Kinematic vorticity and strain rate patterns associated with ductile extrusion in the Chelmos Shear Zone (External Hellenides, Greece), Tectonophysics, 338, 59–77, 2001.

Wiesinger, M., Neubauer, F., and Handler, R.: Exhumation of the Saualpe eclogite unit, Eastern Alps: constraints from $^{40}Ar/^{39}Ar$ ages, Miner. Petrol., 88, 149–180, 2006.

Zanchetta, S., D'Adda, P., Zanchi, A., Barberini, V., and Villa, I. M.: Cretaceous-Eocene compression in the central Southern Alps (N Italy) inferred from $^{40}Ar/^{39}Ar$ dating of pseudotachylytes along regional thrust faults, J. Geodyn., 51, 245–263, 2011.

Zanchetta, S., Garzanti, E., Doglioni, C., and Zanchi, A.: The Alps in the Cretaceous: a doubly vergent pre-collisional orogen, Terra Nova, 24, 351–356, 2012.

Zanchetta, S., Poli, S., Rubatto, D., Zanchi, A., and Bove, G.: Evidence for deep subduction of Austroalpine crust (Texel Complex, NE Italy), Rend. Fis. Acc. Lincei., 24, 163–176, https://doi.org/10.1007/s12210-013-0239-z, 2013.

Zanchetta, S., Malusà, M. G., and Zanchi, A.: Precollisional development and Cenozoic evolution of the Southalpine retrobelt (European Alps), Lithosphere, 7, 662–681, 2015.

Zantedeschi, C.: Geocronologia Rb–Sr sugli gneiss granitoidi del Complesso di Parcines (Alto Adige Occidentale), Mem. Sci. Geol., 43, 319–329, 1991.